at 29μC. *elav-GS/+* served as a control. Female adults ($n=119$–121) were fed yeast paste containing 25 μg/mL RU486. Expression of DG2 shortened lifespan compared with the control (DG2 *vs.* Control, $p<0.01$; dFoxO, DG2 *vs.* Control, $p<0.0001$). (**F**) Flies from each genotype ($n=119$–122) were subjected to survival assays as in (**E**). Pan-neuronal expression of dFoxO SA alone had no significant effect on lifespan when compared with that of dFoxO. Co-expression of dFoxO SA with DG2 failed to attenuate the effect of dFoxO-DG2 combination on lifespan (dFoxO SA, DG2 *vs.* dFoxO, DG2; $p=0.485$).
doi:10.1371/journal.pone.0030958.g006

that DG2 has more complex functions in gene regulation. For example, DG2 might modulate another transcription regulator through phosphorylation along with dFoxO.

Activation of the NOS-sGC pathway leads to increased cGMP levels [26], which in turn has physiological consequences by regulating cGMP effector proteins such as cGMP-regulated ion channels, cGMP-regulated phosphodiesterases, and cGKs [25,27]. It is widely appreciated that cGKs have a variety of roles in tissues, and in the central nervous system. For instance, cGKs regulate neurotransmitter release/uptake and receptor trafficking, neuronal differentiation and axon guidance, synaptic plasticity and memory through the phosphorylation of substrates [27,28,29]. There are two cGK isoforms, cGKI α/β and cGKII, in vertebrates. While cGKI α/β is cytosolic and mainly found in the cerebellum, cerebral cortex, hippocampus, hypothalamus, and olfactory bulb of the brain, cGKII is located in the cellular membranes and widely distributed in the brain [30,31,32]. Here, we demonstrated that cGKII is abundantly expressed in DA neurons in the substantia nigra of the murine midbrain, suggesting that cGKII has a pathogenic role similar to DG2.

What signal mediates stimulation of cGMP synthesis and subsequent cGKII activation in PD remains unclear. The activation of microglia is believed to be one of the pathological processes [33,34], which might begin with the release of aggregated proteins such as oligomeric α-synuclein from neurons into the extracellular space [35]. Inflammation will be amplified by microglial activation and the release of proinflammatory cytokines and inducible NOS [5]. Similarly, dNOS, the only NOS orthologue in *Drosophila*, is involved in an immune response [36]. Thus, inducible NOS responding early to inflammation could be a trigger of the cGKII-FoxO-mediated neurotoxic pathway in humans. In this context, pathogenic LRRK2 with increased kinase activity might potentiate the above pathogenic mechanism. We found that cGKII physically interacts with LRRK2 (Fig. S9), and that they are co-localized at the endosomes (Fig. S10) although our current study suggests LRRK2 and cGKII act independently in the context of FoxO activation. However, we observed that co-expression of cGKII KD and LRRK2 3KD partially stimulates FoxO (Fig. 4B). These kinases have been reported to form a dimmer when activated [29,37,38]. Thus overexpression of kinase-dead forms of cGKII and LRRK2 may accidentally recruit and activate the endogenous kinases in 293T cells although we could not detect the endogenous expression of cGKII in this cell line.

The involvement of NO signaling in PD has been suggested by the findings of higher levels of nNOS and iNOS in the nigrostriatal region and basal ganglia in post mortem PD brains [3,4]. The emerging evidence for pathogenic roles of microglia and astrocytes in PD now supports the idea that glia-induced inflammation and NO production promote the disease's development. However, most studies with post mortem samples or PD models showed only that NO could be a generator of oxidative stress since NO is a free radical involved in a wide range of physiologic events [39]. A very recent study on rodent models of PD have shown that specific inhibition of sGC-cGMP signaling improves basal ganglia dysfunction and motor symptoms, suggesting that NO signaling could act specifically on PD etiology [40]. Our study here provides the possibility that NO signaling downstream to cGK along with FoxO has a pathogenic role in PD.

The relationship between the NO signal and FoxO has been pointed out in a report on a tail suspension-induced model of muscle atrophy, where nNOS-NO is suggested to induce muscle atrophy by upregulating the muscle-specific E3 ubiquitin ligases MuRF-1 and atrogin-1/MAFbx through FoxO activation. Since, the AKT signal is not involved in this mechanism, the molecular mechanism by which FoxO is regulated by nNOS-NO remains unknown [41]. Considering our finding regarding neurodegeneration, cGK may regulate FoxO as a mediator of the NO signal in the atrophic muscles as well. Studies have shown that cGK

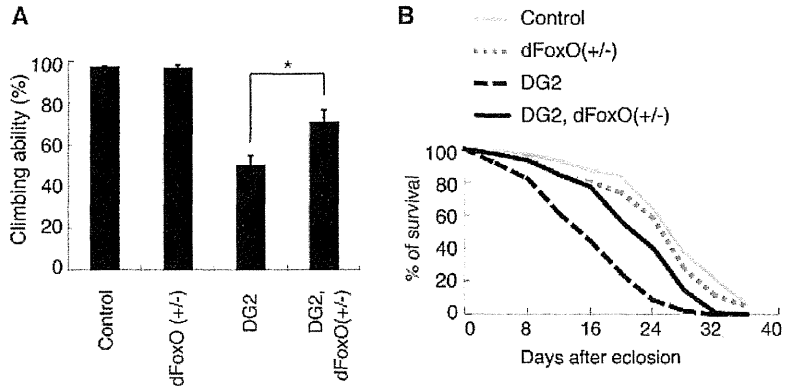

Figure 7. Reduction of endogenous dFoxO activity suppresses DG2-mediated toxicity. (**A**) The climbing activity was measured as in Figure 6C. The values represent means ± SE for 20 trials in three independent experiments (*, $p<0.05$). (**B**) Survival assays of female adults ($n=105$–106) were performed as in Figure 6E. DG2 *vs.* DG2, dFoxO (+/−), $p<0.01$; DG2, dFoxO (+/−) *vs.* Control, $p<0.01$. The genotypes are: *elav-GS/+* (Control), *UAS-DG2; elav-GS* (DG2), *elav-GS/dFoxO*^{21} (dFoxO (+/−)), *UAS-DG2; elav-GS/dFoxO*^{21} (DG2, dFoxO (+/−)).
doi:10.1371/journal.pone.0030958.g007

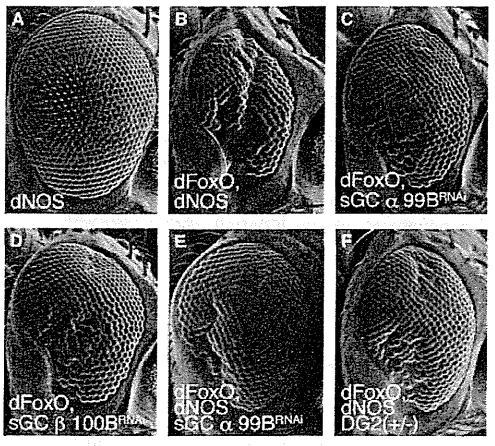

Figure 8. NO signal is involved in FoxO-mediated neurodegeneration. (A–D) SEM images of the eyes of flies expressing the indicated genes. The genotypes are: *GMR-Gal4/UAS-dNOS* **(A)**, *GMR-Gal4, UAS-dFoxO/UAS-dNOS* **(B)**, *GMR-Gal4, UAS-dFoxO; UAS-sGCα99B^{RNAi}* **(C)**, *GMR-Gal4, UAS-dFoxO; UAS-sGCβ100B^{RNAi}* **(D)**, *GMR-Gal4, UAS-dFoxO/UAS-dNOS; UAS-sGCα99B^{RNAi}* **(E)**, *GMR-Gal4, UAS-dFoxO/UAS-dNOS, DG2^{k04703}* **(F)**.
doi:10.1371/journal.pone.0030958.g008

indirectly activates FoxO4 through activation of the JNK pathway [42,43], which provides anti-tumor effects in colon cancer cells. Although the proposed sites of phosphorylation by JNK do not appear to be conserved in dFoxO, there is substantial evidence that JNK-FoxO regulates different cellular processes including anti-aging and cell death in *Drosophila* [44,45,46]. Thus, DG2 could also stimulate the JNK pathway in conjunction with FoxO, widely affecting a variety of cellular mechanisms. This idea could explain why the FoxO SA mutant failed to suppress the DG2-mediated decrease in lifespan of *Drosophila* (Fig. 6E and F).

Although more studies are needed in mammalian systems, our finding of a novel link between the NO signal and FoxO in neurodegeneration suggests that appropriate pharmacological control of the NO pathway would prevent or diminish pathological problems in PD.

Materials and Methods

Drosophila genetics

The *Drosophila* cultures and crosses were performed on standard fly food containing yeast, cornmeal and molasses, and flies were raised at 25ºC unless otherwise stated. General fly stocks and *GAL4* lines were obtained from the Bloomington *Drosophila* stock center. These flies have been described previously: *UAS-dFoxO* [47], *UAS-dFoxO S259A* [16], *UAS-DG1* [18], *UAS-DG2* [18], *UAS-dNOS* [48], *UAS-hLRRK2 WT* [49], *UAS-hLRRK2 I2020T* [49], *UAS-dLRRK WT* [14], *UAS-dLRRK I1915T* [14], *UAS-dLRRK 3KD* [14], *e03680* (*dLRRK null*) [14], *elav*-GeneSwitch [50], *UAS hipo/MST* [51], *UAS-dIKKβ* [52], *UAS-CKIα RNAi* [53], *dFoxO^{21}* [54], *dNOS$^{\Delta 15}$* [55], *UAS-AKT1* (Bloomington stock #8191), *UAS-CDK1-Myc* (#6642), *UAS-CDK2-Myc* (#6634), *UAS-bsk/JNK* (#6407), *mnb^{EY14320}/DYRK1^{EY14320}* (#21430), *CkIα^{EP1555}* (#17009, [56]), *DG2^{k04703}* (#10382), *UAS-sGCα99B^{RNAi}* (#28748), *UAS-sGCβ100B^{RNAi}* (#28786), *hid^{I}* (#631), *DIAP^{1}* (#618), and *UAS-Dronc ^{RNAi}* (NIG-fly 8091R-2 III). *UAS-human cGKII* was generated in the Davies lab.

Antibodies

The anti-α-Tubulin (DM1A), anti-β-Tubulin (Tub2.1) and anti-FLAG (M2) antibodies were purchased from Sigma-Aldrich. The anti-FoxO1 (#9454) antibody was obtained from Cell Signaling Technology. The anti-Myc (4A6), anti-Actin (MAB1501) and anti-phospho-FoxO1 (Ser319, 51136-1) antibodies were purchased from Millipore, Chemicon and Signalway, respectively. The rabbit anti-*Drosophila* TH and anti-dFoxO polyclonal antibody has been described previously [16,57]. Anti-cGKII [30] and anti-cGKIα [31] were kindly provided by Drs. M. Hoffmeister and P. Weinmeister, respectively. The rabbit anti-hLRRK2 polyclonal antibodies were raised against GST-hLRRK2 (823–1004 aa) and (1868–2138 aa) produced in *E. coli* BL21(DE3)pLysS (Novagen).

Plasmids

cDNA for human cGKIα and rat cGKII, kindly provided by Drs. S. Lohmann and A. Smolenski, was subcloned into pcDNA3-Myc or pcDNA3-FLAG. A plasmid for EGFP-FoxO1 was a kind gift from Dr. T. Unterman. A plasmid for AKT-PH-GFP was from Addgene. Plasmids for *FLAG-hLRRK2* and *FLAG-dLRRK* [14], mouse FoxO1, and human 4E-BP1 and the luciferase reporter plasmid for FoxO (TK.IRS3) have been reported elsewhere [58]. The plasmid for DG2 was also reported previously [18]. Mutations were introduced using the QuikChange II XL Site-directed mutagenesis kit (Stratagene). Although we used mouse FoxO1 cDNA as a mammalian FoxO gene, the numbering is based on the human sequence to avoid confusion. Thus, Ser149–152, Ser181 and Ser316 in mouse FoxO1 correspond to Ser152–155, Ser184 and Ser319 in human FoxO1, respectively. The kinase-dead form of rat cGKII (cGKII KD) was generated by replacing Asp549 with alanine, which corresponds to bovine cGKIα D501A mutation described in [59].

In vitro phosphorylation assay

FLAG-cGKII, FLAG-hLRRK2, and mock fractions immunopurified from transfected and mock-transfected 293T cells were used as kinase sources. The same batches of kinase fractions were used throughout the experiments, and their quality and quantity was confirmed by western blot as shown in Fig. 5B and S6. Five micrograms of GST-FoxO1, mutant forms of GST-FoxO1 and His-4E-BP1 were incubated with the kinase sources in a kinase reaction buffer containing 20 mM HEPES (pH7.4), 15 mM $MgCl_2$, 5 mM EGTA, 0.1% Triton X-100, 0.5 mM DTT, 1 mM β-glycerolphosphate, and 2.5 μCi [γ-^{32}P]-ATP in the presence or absence of 30 μM cGMP for 30 min at 30ºC. The reaction mixture was then suspended in SDS sample buffer and subjected to SDS-PAGE and autoradiography.

Cell culture, immunopurification and western blotting

Transfection of human embryonic kidney 293T and *Drosophila* Schneider 2 (S2) cells, immunopurification from the transfected cell or mouse brain lysate, and western blotting were performed as described previously [16,60,61]. Flp-In T-REx-293 cell line

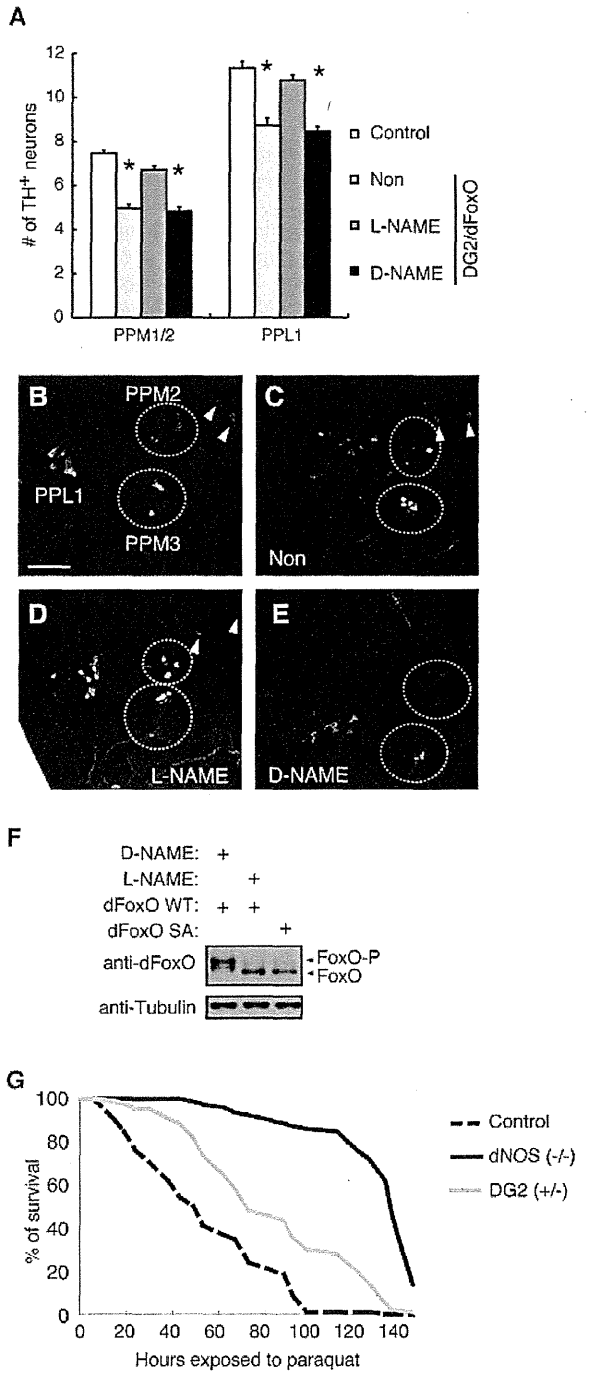

Figure 9. Inhibition of NO signal improves DG2-dFoxO-mediated DA neurodegeneration. **(A)** Newly eclosed normal *w-* flies (Control) or transgenics harboring *elav-GS>UAS-dFoxO/UAS-DG2* ($n=22$ in each) were fed a yeast paste containing 50 μg/mL_ RU486 with or without 10 mM L-NAME or D-NAME every 4 days at 29uC. The graph presents the number of PPM 1/2 and PPL1 clusters of TH-positive neurons in 20-day-old adult flies. PPM1 and PPM2 clusters were counted together. Data are presented as the mean ± SE for three experiments (*, $p<0.05$ *vs.* Control). PPL, the protocerebral posterior lateral. Non; RU486 only. **(B)** A representative image of TH-positive PPL1, PPM1, PPM2 (upper circle) and PPM3 (lower circle) neurons of a wild-type *w-* adult fly. Arrowheads indicate a pair of PPM1 neurons. Bar=50 μm. **(C–E)** Representative images of TH-positive neurons treated as in **A**. **(F)** Brain tissues of dFoxO transgenic flies treated with L-NAME or D-NAME were subjected to western blot analysis with anti-dFoxO. dFoxO SA mutant was also included as a non-phosphorylated control. Transgenes were expressed by the *elav-GS* driver. **(G)** Reduction of dNOS and DG2 activities confers stress resistance against 2 mM paraquat treatment. dNOS (−/−) *vs.* Control, $p<0.0001$; DG2 (+/−) *vs.* Control, $p<0.01$. The genotypes are: *w-* (Control), $dNOS^{\Delta 15}/dNOS^{\Delta 15}$ (dNOS (−/−)), $DG2^{k04703}$/+ (DG2 (+/−)).
doi:10.1371/journal.pone.0030958.g009

harboring doxycycline-inducible EGFP-FoxO1 gene was generated according to the manufacturer's instructions (Invitrogen).

Scanning Electron Microscopy (SEM)

Adult flies were processed as described previously [14]. SEM images were obtained at The Biomedical Research Core of Tohoku University Graduate School of Medicine.

Lifespan and survival assays

Twenty female adult flies per vial were maintained at 29uC, transferred to fresh fly food vials containing 250 μl of yeast paste and 25 μg/ml of RU486, and scored for survival every 4 days. To control for isogeny, all fly lines were backcrossed to the w^- wild-type background for six generations or were generated on the w^- background, and thus have matched genetic backgrounds. Survival assays of flies treated with 2 mM paraquat were performed as described previously [14].

Climbing assay

The climbing assay was performed as described previously [14]. Briefly, twenty flies were placed in a plastic vial (18.6 cm in height6 3.5 cm^2 in area) and gently tapped to bring them down to the bottom of the vial. Flies were given 18 s to climb and the number of flies more than 6 cm from the bottom was counted. Twenty trials were performed for the same set of flies. Flies at 20 days of age were left untreated or treated with 1 mM L-DOPA for 4 days, then subjected to climbing assays.

Whole-mount immunostaining

Total number of TH-positive neurons were calculated following whole-mount immunostaining of brain samples as described previously [57]. All immunohistochemical analyses were performed using a Carl Zeiss laser scanning microscope system.

Statistical analysis

The one-way repeated measures ANOVA was used to determine significant differences between multiple groups unless otherwise indicated. If a significant result was achieved ($p<0.05$), the means of the control and the specific test group were analyzed using the Tukey-Kramer test. For lifespan assays, a Kaplan-Meier analysis with the log-rank test was performed.

Supporting Information

Figure S1 Evaluation of mnb and dgl expression in $mnb^{EY14320}$ and UAS-DG1 fly lines in the presence of the GAL4 driver. Total RNA was extracted from the *Da-Gal4* crosses. The *mnb*, an orthologue of mammalian *DYRK1*, *dgl* and *rp49* transcript levels were measured by real-time PCR. *mnb* (A) or *dgl* (B) transcript levels normalized to those of *rp49* are presented. (TIF)

Figure S2 DG1 does not exacerbate dFoxO-mediated eye degeneration. Transgenic expression of DG2 alone did not produce eye degeneration, and DG1 had little effect on the eye phenotype caused by expression of dFoxO (when compared to Figure 2B). (C) The numbers of ommatidia per fly eye (from 5 flies) were quantified. *, $p<0.05$; N.S., non-significant. The genotypes are: *UAS-DG2; GMR-Gal4* (A), *GMR-Gal4, UAS-dFoxO; UAS-DG1* (B), *GMR-Gal4/UAS-EGFP* (EGFP), *GMR-Gal4, UAS-dFoxO/UAS-EGFP* (dFoxO, EGFP), *GMR-Gal4, UAS-dFoxO; UAS-DG1* (dFoxO, DG1) (C).
(TIF)

Figure S3 cGKII does not form a stable complex with cGKIa or FoxO1. Lysate from 293T cells transfected with cGKII-FLAG together with or without FoxO1-Myc or cGKIα-Myc was immunoprecipitated with anti-FLAG antibody (FLAG-IP). Immunoprecipitates and total soluble lysates (Lysate) were analyzed by western blotting.
(TIF)

Figure S4 cGKII is expressed in DA neurons of the murine midbrain. Immunolocalization of cGKIα (green in A, C), cGKII (green in B, D) and TH (red) in coronal sections of the substantia nigra (A, B) and striatum (C, D) of the brain. Yellow in B indicates the expression of cGKII in TH-positive neuronal processes (arrow heads) as well as cell bodies (arrows). The right columns of each panel show high-magnification images of the boxes in the left columns. Scale bars = 20 μm.
(TIF)

Figure S5 Mutations of cGKII phosphorylation sites localized in FoxO1-N do not affect the FoxO-transcriptional activity. (A) Reported phosphorylation sites in FoxO1 by cGKI are depicted [22]. Phospho-resistant mutants, where the indicated Ser or Thr residues are replaced with alanine, are also shown. (B) The phospho-signal by cGKII was decreased in GST-FoxO-4M compared with GST-FoxO-N WT (lane 3 *vs.* lane 2), but was no longer decreased in GST-FoxO-5M (data not shown), suggesting that S184 is not a major phosphorylation site by cGKII. (C) The FoxO1 4M mutation had little effect on FoxO-transcriptional activity stimulated by cGKII and/or LRRK2. (D) Effects of the 4M mutation on physical interaction between FoxO1 and 14-3-3ε were estimated in 293T cells. FoxO1-Myc-6x His was pulled down with Ni-NTA beads from the lysate of cells expressing the indicated transgenes.
(TIF)

Figure S6 The Ser319 site of FoxO1 is not a major target of cGKI in vitro. *In vitro* kinase assay was performed as in Fig. 5. P3 SA; a P3 mutant in which the Ser319 residue is replaced with alanine. Autophosphorylation signals of cGKII and cGKI are also shown in the upper panel.
(TIF)

Figure S7 cGKII phosphorylates LRRK2. (A) cGKII WT but not cGKII KD phosphorylates LRRK2 3KD (lane 9) as well as LRRK2 WT (lane 6) in *in vitro* kinase assay. *In vitro* kinase assay was performed as in Fig. 5. (B) Western blot analysis with anti-FLAG indicates similar amounts of FLAG-LRRK2 WT and FLAG-LRRK2 3KD were used in the kinase assay.
(TIF)

Figure S8 Hid is not a major gene responsible for FoxO-DG2-mediated optic degeneration. Introduction of loss-of-function alleles of a pro-apoptotic gene *hid* (B) or anti-apoptotic *DIAP* (C), or knockdown of Dronc, a caspase downstream of Hid (D), had little effects on the eye phenotype by co-expression of dFoxO and DG2 (A). The genotypes are: *UAS-DG2; GMR-Gal4, UAS-dFoxO* (A), *UAS-DG2; GMR-Gal4, UAS-dFoxO; hid^{1}* (B), *UAS-DG2; GMR-Gal4, UAS-dFoxO; DIAP^{1}* (C), *UAS-DG2; GMR-Gal4, UAS-dFoxO; UAS-Dronc^{RNAi}* (D). (E) Real-time RT-PCR analysis for *hid* and *4E-BP* was performed using total RNA from S2 cells expressing the indicated gene combinations. Values are presented as the mean ± SE for three repeated experiments. *, $p<0.05$ *vs.* Control.
(TIF)

Figure S9 cGKII is associated with LRRK2. (A) Lysate from 293T cells transfected with FLAG-tagged LRRK2 with or without Myc-cGKII was immunoprecipitated with anti-FLAG antibody (FLAG-IP). Immunoprecipitates and total soluble lysates (lysate) were analyzed by western blotting. (B) The diagram represents LRRK2 and the mutants used to determine the cGKII-binding domain. Numbers in parentheses indicate corresponding amino acid residues of LRRK2. LRR, leucine-rich repeat; ROC, Ras in complex proteins; COR, C-terminal of Roc; Kinase, protein kinase domain; WD40, WD40 domain. (C) Immunoprecipitation-western blot analysis as in (A) revealed cGKII to be associated with LRRK2-C. (D) cGKII associates strongly with LRRK2-C_3, and weakly with LRRK2-C_1 and -C_2. (E) Endogenous interaction of cGKII but not cGKIα with LRRK2 in brain tissue. Mouse brain tissues were lysed as described [60], then the supernatant fractions were immunoprecipitated (IP) with anti-cGKII or anti-cGKIα antibodies. The co-precipitated LRRK2 was detected by western blotting using anti-LRRK2 antibody. 293T lysate expressing FLAG-LRRK2 or FLAG-cGKII served as a positive control.
(TIF)

Figure S10 cGKII is co-localized with LRRK2 at the endosomes. (A) Immunolocalization of cGKII and LRRK2 in 293T cells expressing FLAG-LRRK2 and Myc-cGKII. cGKII and LRRK2 were visualized with anti-Myc (green) or anti-LRRK2 antibody (red). LRRK2 is localized at the Rab-positive endosomes (data not shown). cGKII is localized at the cytoplasmic membrane and partly in the cytoplasmic compartments. cGKII and LRRK2 were co-localized at the Rab-positive endosomes (yellow). Scale bar = 10 μm. (B–E) Immunolocalization of cGKII (red) in 293T cells expressing Myc-cGKII and EGFP-tagged Rabs (green). Cytosolic cGKII is located mainly at Rab4- and Rab5-positive endosomes, and partially at Rab7- or Rab11-positive endosomes.
(TIF)

Acknowledgments

We thank A. Yasui, S. Nakajima, S. Kanno and M. Kaji for excellent technical support and equipment, and T. Furuyama, T. Unterman, G. Halder, K.V. Anderson, J. Jiang, T. Osterwalder S. Lohmann, A. Smolenski, M. Hoffmeister, F. Hofmann, P. Weinmeister, PH. O'Farrell and M. Fukuda for the generous supply of materials.

Author Contributions

Conceived and designed the experiments: TK YI. Performed the experiments: TK TS YI. Analyzed the data: TK YI. Contributed reagents/materials/analysis tools: TS SD HI KH RT NH. Wrote the paper: YI.

References

1. Steinert JR, Chernova T, Forsythe ID (2010) Nitric oxide signaling in brain function, dysfunction, and dementia. Neuroscientist 16: 435–452.
2. West AR, Tseng KY (2011) Nitric Oxide-Soluble Guanylyl Cyclase-Cyclic GMP Signaling in the Striatum: New Targets for the Treatment of Parkinson's Disease? Front Syst Neurosci 5: 55.
3. Hunot S, Boissiere F, Faucheux B, Brugg B, Mouatt-Prigent A, et al. (1996) Nitric oxide synthase and neuronal vulnerability in Parkinson's disease. Neuroscience 72: 355–363.
4. Eve DJ, Nisbet AP, Kingsbury AE, Hewson EL, Daniel SE, et al. (1998) Basal ganglia neuronal nitric oxide synthase mRNA expression in Parkinson's disease. Brain Res Mol Brain Res 63: 62–71.
5. Liberatore GT, Jackson-Lewis V, Vukosavic S, Mandir AS, Vila M, et al. (1999) Inducible nitric oxide synthase stimulates dopaminergic neurodegeneration in the MPTP model of Parkinson disease. Nat Med 5: 1403–1409.
6. Muramatsu Y, Kurosaki R, Watanabe H, Michimata M, Matsubara M, et al. (2003) Cerebral alterations in a MPTP-mouse model of Parkinson's disease an immunocytochemical study. J Neural Transm 110: 1129–1144.
7. Dreyer J, Schleicher M, Tappe A, Schilling K, Kuner T, et al. (2004) Nitric oxide synthase (NOS)-interacting protein interacts with neuronal NOS and regulates its distribution and activity. J Neurosci 24: 10454–10465.
8. Paisan-Ruiz C, Jain S, Evans EW, Gilks WP, Simon J, et al. (2004) Cloning of the gene containing mutations that cause PARK8-linked Parkinson's disease. Neuron 44: 595–600.
9. Zimprich A, Biskup S, Leitner P, Lichtner P, Farrer M, et al. (2004) Mutations in LRRK2 cause autosomal-dominant parkinsonism with pleomorphic pathology. Neuron 44: 601–607.
10. Healy DG, Falchi M, O'Sullivan SS, Bonifati V, Durr A, et al. (2008) Phenotype, genotype, and worldwide genetic penetrance of LRRK2-associated Parkinson's disease: a case-control study. Lancet Neurol 7: 583–590.
11. Mata IF, Wedemeyer WJ, Farrer MJ, Taylor JP, Gallo KA (2006) LRRK2 in Parkinson's disease: protein domains and functional insights. Trends Neurosci 29: 286–293.
12. West AB, Moore DJ, Biskup S, Bugayenko A, Smith WW, et al. (2005) Parkinson's disease-associated mutations in leucine-rich repeat kinase 2 augment kinase activity. Proc Natl Acad Sci U S A 102: 16842–16847.
13. Gloeckner CJ, Kinkl N, Schumacher A, Braun RJ, O'Neill E, et al. (2006) The Parkinson disease causing LRRK2 mutation I2020T is associated with increased kinase activity. Hum Mol Genet 15: 223–232.
14. Imai Y, Gehrke S, Wang HQ, Takahashi R, Hasegawa K, et al. (2008) Phosphorylation of 4E-BP by LRRK2 affects the maintenance of dopaminergic neurons in Drosophila. Embo J 27: 2432–2443.
15. Lessing D, Bonini NM (2009) Maintaining the brain: insight into human neurodegeneration from Drosophila melanogaster mutants. Nat Rev Genet 10: 359–370.
16. Kanao T, Venderova K, Park DS, Unterman T, Lu B, et al. (2010) Activation of FoxO by LRRK2 induces expression of proapoptotic proteins and alters survival of postmitotic dopaminergic neuron in Drosophila. Hum Mol Genet 19: 3747–3758.
17. Kalderon D, Rubin GM (1989) cGMP-dependent protein kinase genes in Drosophila. J Biol Chem 264: 10738–10748.
18. MacPherson MR, Lohmann SM, Davies SA (2004) Analysis of Drosophila cGMP-dependent protein kinases and assessment of their in vivo roles by targeted expression in a renal transporting epithelium. J Biol Chem 279: 40026–40034.
19. Jarchau T, Hausler C, Markert T, Pohler D, Vanderkerckhove J, et al. (1994) Cloning, expression, and in situ localization of rat intestinal cGMP-dependent protein kinase II. Proc Natl Acad Sci U S A 91: 9426–9430.
20. Kulaksiz H, Rehberg E, Stremmel W, Cetin Y (2002) Guanylin and functional coupling proteins in the human salivary glands and gland tumors: expression, cellular localization, and target membrane domains. Am J Pathol 161: 655–664.
21. Yuasa K, Yamagami S, Nagahama M, Tsuji A (2008) Trafficking of cGMP-dependent protein kinase II via interaction with Rabl1. Biochem Biophys Res Commun 374: 522–526.
22. Bois PR, Brochard VF, Salin-Cantegrel AV, Cleveland JL, Grosveld GC (2005) FoxO1a-cyclic GMP-dependent kinase I interactions orchestrate myoblast fusion. Mol Cell Biol 25: 7645–7656.
23. Bicker G (2007) Pharmacological approaches to nitric oxide signalling during neural development of locusts and other model insects. Arch Insect Biochem Physiol 64: 43–58.
24. Davies S (2000) Nitric oxide signalling in insects. Insect Biochem Mol Biol 30: 1123–1138.
25. Davies SA (2006) Signalling via cGMP: lessons from Drosophila. Cell Signal 18: 409–421.
26. Wang X, Robinson PJ (1997) Cyclic GMP-dependent protein kinase and cellular signaling in the nervous system. J Neurochem 68: 443–456.
27. Hofmann F, Feil R, Kleppisch T, Schlossmann J (2006) Function of cGMP-dependent protein kinases as revealed by gene deletion. Physiol Rev 86: 1–23.
28. Feil R, Hofmann F, Kleppisch T (2005) Function of cGMP-dependent protein kinases in the nervous system. Rev Neurosci 16: 23–41.
29. Serulle Y, Zhang S, Ninan I, Puzzo D, McCarthy M, et al. (2007) A GluR1-cGKII interaction regulates AMPA receptor trafficking. Neuron 56: 670–688.
30. de Vente J, Asan E, Gambaryan S, Markerink-van Ittersum M, Axer H, et al. (2001) Localization of cGMP-dependent protein kinase type II in rat brain. Neuroscience 108: 27–49.
31. Feil S, Zimmermann P, Knorn A, Brummer S, Schlossmann J, et al. (2005) Distribution of cGMP-dependent protein kinase type I and its isoforms in the mouse brain and retina. Neuroscience 135: 863–868.
32. Geiselhoringer A, Gaisa M, Hofmann F, Schlossmann J (2004) Distribution of IRAG and cGKI-isoforms in murine tissues. FEBS Lett 575: 19–22.
33. McGeer PL, Itagaki S, Boyes BE, McGeer EG (1988) Reactive microglia are positive for HLA-DR in the substantia nigra of Parkinson's and Alzheimer's disease brains. Neurology 38: 1285–1291.
34. Glass CK, Saijo K, Winner B, Marchetto MC, Gage FH (2010) Mechanisms underlying inflammation in neurodegeneration. Cell 140: 918–934.
35. Roodveldt C, Christodoulou J, Dobson CM (2008) Immunological features of alpha-synuclein in Parkinson's disease. J Cell Mol Med 12: 1820–1829.
36. Foley E, O'Farrell PH (2003) Nitric oxide contributes to induction of innate immune responses to gram-negative bacteria in Drosophila. Genes Dev 17: 115–125.
37. Berger Z, Smith KA, Lavoie MJ (2010) Membrane localization of LRRK2 is associated with increased formation of the highly active LRRK2 dimer and changes in its phosphorylation. Biochemistry 49: 5511–5523.
38. Greggio E, Zambrano I, Kaganovich A, Beilina A, Taymans JM, et al. (2008) The Parkinson disease-associated leucine-rich repeat kinase 2 (LRRK2) is a dimer that undergoes intramolecular autophosphorylation. J Biol Chem 283: 16906–16914.
39. Aquilano K, Baldelli S, Rotilio G, Ciriolo MR (2008) Role of nitric oxide synthases in Parkinson's disease: a review on the antioxidant and anti-inflammatory activity of polyphenols. Neurochem Res 33: 2416–2426.
40. Tseng KY, Caballero A, Dec A, Cass DK, Simak N, et al. (2011) Inhibition of Striatal Soluble Guanylyl Cyclase-cGMP Signaling Reverses Basal Ganglia Dysfunction and Akinesia in Experimental Parkinsonism. PLoS One 6: e27187.
41. Suzuki N, Motohashi N, Uezumi A, Fukada S, Yoshimura T, et al. (2007) NO production results in suspension-induced muscle atrophy through dislocation of neuronal NOS. J Clin Invest 117: 2468–2476.
42. Soh JW, Kazi JU, Li H, Thompson WJ, Weinstein IB (2008) Celecoxib-induced growth inhibition in SW480 colon cancer cells is associated with activation of protein kinase G. Mol Carcinog 47: 519–525.
43. Kwon IK, Wang R, Thangaraju M, Shuang H, Liu K, et al. (2010) PKG inhibits TCF signaling in colon cancer cells by blocking beta-catenin expression and activating FOXO4. Oncogene 29: 3423–3434.
44. Lee KS, Iijima-Ando K, Iijima K, Lee WJ, Lee JH, et al. (2009) JNK/FOXO-mediated neuronal expression of fly homologue of peroxiredoxin II reduces oxidative stress and extends life span. J Biol Chem 284: 29454–29461.
45. Hong YK, Lee NG, Lee MJ, Park MS, Choi G, et al. (2009) dXNP/DATRX increases apoptosis via the JNK and dFOXO pathway in Drosophila neurons. Biochem Biophys Res Commun 384: 160–166.
46. Wang MC, Bohmann D, Jasper H (2005) JNK extends life span and limits growth by antagonizing cellular and organism-wide responses to insulin signaling. Cell 121: 115–125.
47. Puig O, Marr MT, Ruhf ML, Tjian R (2003) Control of cell number by Drosophila FOXO: downstream and feedback regulation of the insulin receptor pathway. Genes Dev 17: 2006–2020.
48. McGettigan J, McLennan RK, Broderick KE, Kean L, Allan AK, et al. (2005) Insect renal tubules constitute a cell-autonomous immune system that protects the organism against bacterial infection. Insect Biochem Mol Biol 35: 741–754.
49. Venderova K, Kabbach G, Abdel-Messih E, Zhang Y, Parks RJ, et al. (2009) Leucine-Rich Repeat Kinase 2 interacts with Parkin, DJ-1 and PINK-1 in a Drosophila melanogaster model of Parkinson's disease. Hum Mol Genet 18: 4390–4404.
50. Osterwalder T, Yoon KS, White BH, Keshishian H (2001) A conditional tissue-specific transgene expression system using inducible GAL4. Proc Natl Acad Sci U S A 98: 12596–12601.
51. Udan RS, Kango-Singh M, Nolo R, Tao C, Halder G (2003) Hippo promotes proliferation arrest and apoptosis in the Salvador/Warts pathway. Nat Cell Biol 5: 914–920.
52. Lu Y, Wu LP, Anderson KV (2001) The antibacterial arm of the drosophila innate immune response requires an IkappaB kinase. Genes Dev 15: 104–110.
53. Jia J, Tong C, Wang B, Luo L, Jiang J (2004) Hedgehog signalling activity of Smoothened requires phosphorylation by protein kinase A and casein kinase I. Nature 432: 1045–1050.
54. Junger MA, Rintelen F, Stocker H, Wasserman JD, Vegh M, et al. (2003) The Drosophila forkhead transcription factor FOXO mediates the reduction in cell number associated with reduced insulin signaling. J Biol 2: 20.
55. Yakubovich N, Silva EA, O'Farrell PH (2010) Nitric oxide synthase is not essential for Drosophila development. Curr Biol 20: R141–142.
56. Muller D, Kugler SJ, Preiss A, Maier D, Nagel AC (2005) Genetic modifier screens on Hairless gain-of-function phenotypes reveal genes involved in cell differentiation, cell growth and apoptosis in Drosophila melanogaster. Genetics 171: 1137–1152.
57. Yang Y, Gehrke S, Imai Y, Huang Z, Ouyang Y, et al. (2006) Mitochondrial pathology and muscle and dopaminergic neuron degeneration caused by

inactivation of Drosophila Pink1 is rescued by Parkin. Proc Natl Acad Sci U S A 103: 10793–10798.
58. Zhang X, Gan L, Pan H, Guo S, He X, et al. (2002) Phosphorylation of serine 256 suppresses transactivation by FKHR (FOXO1) by multiple mechanisms. Direct and indirect effects on nuclear/cytoplasmic shuttling and DNA binding. J Biol Chem 277: 45276–45284.
59. Yuasa K, Michibata H, Omori K, Yanaka N (2000) Identification of a conserved residue responsible for the autoinhibition of cGMP-dependent protein kinase Ialpha and beta. FEBS Lett 466: 175–178.
60. Imai Y, Soda M, Inoue H, Hattori N, Mizuno Y, et al. (2001) An unfolded putative transmembrane polypeptide, which can lead to endoplasmic reticulum stress, is a substrate of Parkin. Cell 105: 891–902.
61. Imai Y, Soda M, Takahashi R (2000) Parkin suppresses unfolded protein stress-induced cell death through its E3 ubiquitin-protein ligase activity. J Biol Chem 275: 35661–35664.
62. Kwon Y, Hofmann T, Montell C (2007) Integration of phosphoinositide- and calmodulin-mediated regulation of TRPC6. Mol Cell 25: 491–503.

Saito *et al. Molecular Neurodegeneration* 2012, **7**:50
http://www.molecularneurodegeneration.com/content/7/1/50

MOLECULAR NEURODEGENERATION

RESEARCH ARTICLE Open Access

Hyperpolarization-activated cyclic nucleotide gated channels: a potential molecular link between epileptic seizures and Aβ generation in Alzheimer's disease

Yuhki Saito[1], Tsuyoshi Inoue[2], Gang Zhu[3], Naoki Kimura[1], Motohiro Okada[4], Masaki Nishimura[5], Nobuyuki Kimura[6], Shigeo Murayama[7,8], Sunao Kaneko[9], Ryuichi Shigemoto[10], Keiji Imoto[11] and Toshiharu Suzuki[1*]

Abstract

Background: One of the best-characterized causative factors of Alzheimer's disease (AD) is the generation of amyloid-β peptide (Aβ). AD subjects are at high risk of epileptic seizures accompanied by aberrant neuronal excitability, which in itself enhances Aβ generation. However, the molecular linkage between epileptic seizures and Aβ generation in AD remains unclear.

Results: X11 and X11-like (X11L) gene knockout mice suffered from epileptic seizures, along with a malfunction of hyperpolarization-activated cyclic nucleotide gated (HCN) channels. Genetic ablation of HCN1 in mice and HCN1 channel blockage in cultured Neuro2a (N2a) cells enhanced Aβ generation. Interestingly, HCN1 levels dramatically decreased in the temporal lobe of cynomolgus monkeys (*Macaca fascicularis*) during aging and were significantly diminished in the temporal lobe of sporadic AD patients.

Conclusion: Because HCN1 associates with amyloid-β precursor protein (APP) and X11/X11L in the brain, genetic deficiency of X11/X11L may induce aberrant HCN1 distribution along with epilepsy. Moreover, the reduction in HCN1 levels in aged primates may contribute to augmented Aβ generation. Taken together, HCN1 is proposed to play an important role in the molecular linkage between epileptic seizures and Aβ generation, and in the aggravation of sporadic AD.

Background

Alzheimer's disease (AD) is characterized by progressive memory impairment, which accompanies aging. Genetic and biochemical studies show that the production of amyloid-β peptide (Aβ) largely contributes to the etiology of AD [1]. Aβ is generated from amyloid-β precursor protein (APP) by β- and γ-cleavage of the latter.

The risk of seizure activity is particularly high in AD patients, with an 87-fold increase in subjects with early-onset dementia compared with an age-matched reference population [2-7]. Factors linking seizure activity to Aβ generation in AD patients remain unclear, although epilepsy is believed to result from abnormal regulation of neuronal excitability, which favors hypersynchrony. In addition, increased neuronal activity enhances Aβ production from APP [8-10].

Hyperpolarization-activated cyclic nucleotide gated HCN channels 1–4 (HCN1–4) conduct inward, depolarizing mixed Na^+/K^+ currents and thereby control resting membrane potential, dendritic integration, synaptic transmission, and rhythmic activity in cardiac pacemaker cells and spontaneous firing neurons [11]. Dysregulation of these channels and their hyperpolarization-activated (Ih) currents is strongly implicated in various experimental animal models of epilepsy, as well as in human epilepsy patients [12]. Furthermore, HCN2 co-assembles with the X11-like (X11L) protein [13], which is a metabolic regulator of APP processing [14].

X11 proteins (X11s) comprise a family of three evolutionarily conserved molecules (X11/X11α/Mint1, X11L/

* Correspondence: tsuzuki@pharm.hokudai.ac.jp
[1]Laboratory of Neuroscience, Graduate School of Pharmaceutical Sciences, Hokkaido University, Kita12-Nishi6, Kita-ku, Sapporo 060-0812, Japan
Full list of author information is available at the end of the article

X11β/Mint2, and X11L2/X11γ/Mint3). These proteins bind to the cytoplasmic region of APP in cultured cells and suppress its metabolism [15,16]. Moreover, the metabolism of overexpressed human APP (hAPP) is suppressed in X11 and X11L transgenic mice, along with the generation of Aβ [17-19]. On the other hand, mutant mice lacking X11L ($X11^{+/+}/X11L^{-/-}$ mice) or both X11 and X11L ($X11^{-/-}/X11L^{-/-}$ mice) facilitate amyloidogenic metabolism of endogenous murine APP and exogenous hAPP, including Aβ generation [20-22]. Therefore, inactivation of X11/X11L clearly increases the production of Aβ, potentially contributing to the pathology of AD.

Here, we report that i) $X11^{-/-}/X11L^{-/-}$ mice suffer from spontaneous epileptic seizures along with malfunction of HCN channel activity; ii) HCN1 can form a complex with APP and X11 or X11L in the murine brain; iii) $HCN1^{-/-}$ gene knockout mice show enhanced Aβ generation; iv) overexpression of HCN1 in Neuro2a (N2a) cells decreases Aβ generation, whereas blockage of HCN1 channel activity in N2a cells restores the level of Aβ production; v) the level of HCN1 diminishes significantly in the temporal cortex of cynomolgus monkeys (*Macaca fascicularis*) during aging; and vi) HCN1 levels are significantly reduced in the brains of sporadic AD patients compared with the brains of age-matched healthy subjects.

Given the previous reports and our current observations, we hypothesize that X11 and X11L play an important role in the modulation of HCN channel function, the dysregulation of which correlates with epilepsy. We further hypothesize that the impairment of HCN channels, and in particular HCN1, accompanies with the aberrant production of Aβ, which manifests as neurotoxicity. Thus, HCN1 together with X11 and X11L may provide a molecular link between seizure activity and Aβ generation in AD patients.

Results

Spontaneous epileptic seizures caused by X11 and X11L gene deficiency

Electrocorticograms were recorded in $X11^{+/+}/X11L^{+/+}$ (wild type), $X11^{+/+}/X11L^{-/-}$, $X11^{-/-}/X11L^{+/+}$, and $X11^{-/-}/X11L^{-/-}$ mice. We found that $X11^{-/-}/X11L^{-/-}$ mice suffered from spontaneous epileptic seizures at the age of 13 weeks and over (detailed results are provided in Additional file 1: Figure S1 and Additional file 2: Movies S1, Additional file 3: Movies S2 and Additional file 4: Movies S3). Three out of four $X11^{-/-}/X11L^{-/-}$ mice showed an abnormal electrocorticogram recording within 48 h, namely, the presence of epileptic discharge, which were never observed in $X11^{+/+}/X11L^{+/+}$, $X11^{+/+}/X11L^{-/-}$, or $X11^{-/-}/X11L^{+/+}$

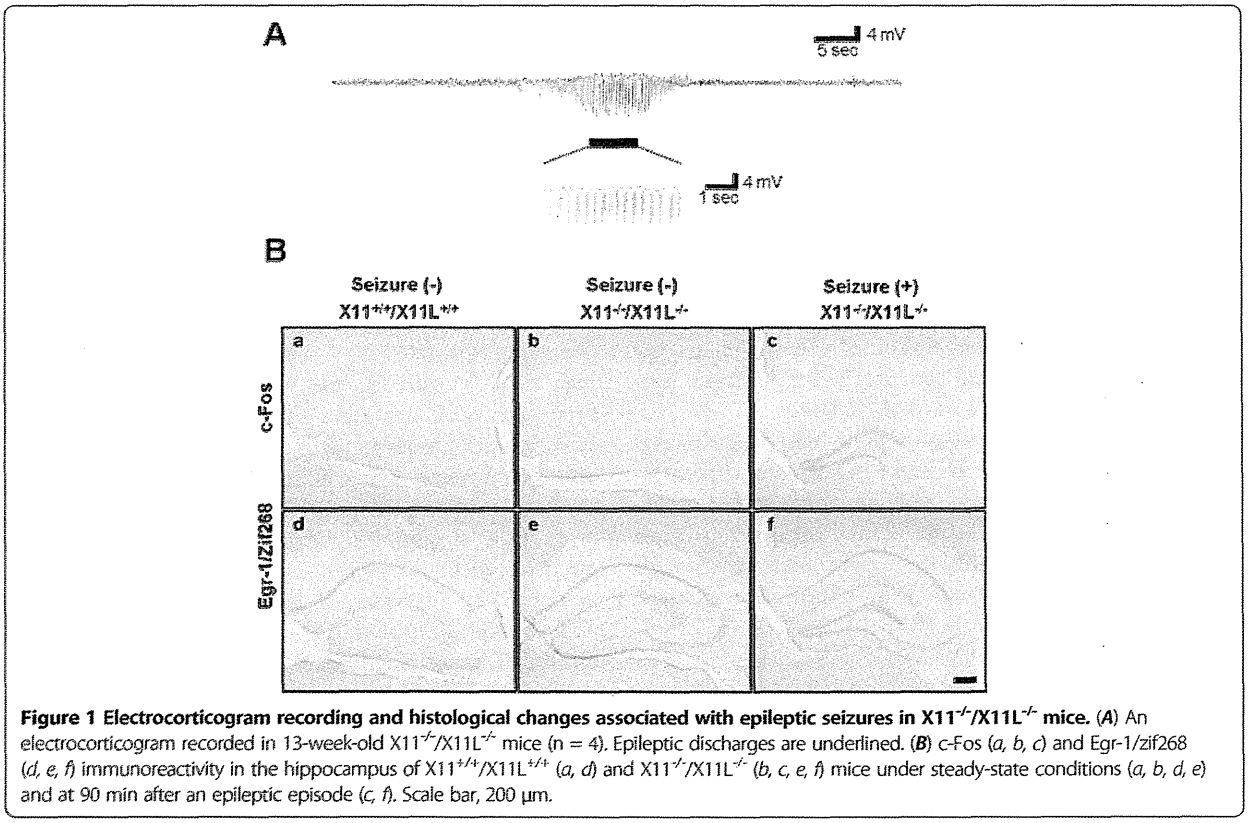

Figure 1 Electrocorticogram recording and histological changes associated with epileptic seizures in $X11^{-/-}/X11L^{-/-}$ mice. (*A*) An electrocorticogram recorded in 13-week-old $X11^{-/-}/X11L^{-/-}$ mice (n = 4). Epileptic discharges are underlined. (*B*) c-Fos (*a, b, c*) and Egr-1/zif268 (*d, e, f*) immunoreactivity in the hippocampus of $X11^{+/+}/X11L^{+/+}$ (*a, d*) and $X11^{-/-}/X11L^{-/-}$ (*b, c, e, f*) mice under steady-state conditions (*a, b, d, e*) and at 90 min after an epileptic episode (*c, f*). Scale bar, 200 μm.

mice (Figure 1, Additional file 1: Figure S1 and Additional file 4: Movie S3). Subsets of $X11^{-/-}/X11L^{-/-}$ mice went into status epilepticus and died.

Seizures are often associated with the augmented expression of immediate-early genes in neurons [23]. We first asked whether such gene activation was observed in $X11^{-/-}/X11L^{-/-}$ mice following epileptic seizures and investigated the involvement of specific brain regions in seizure activity. Brain tissue sections from $X11^{-/-}/X11L^{-/-}$ mice were immunostained for c-Fos, a calcium-dependent immediate-early gene product, and Egr-1/Zif268, an early growth response transcription factor, within 90 min of a seizure event. The brains of these mice showed enhanced expression of both c-Fos and Egr-1/Zif268 in the dentate gyrus (DG) granule cells compared with the brains of $X11^{+/+}/X11L^{+/+}$ and $X11^{-/-}/X11L^{-/-}$ mice (Figure 1B). However, we cannot rule out a possibility that subclinical discharges without aberrant behavior may

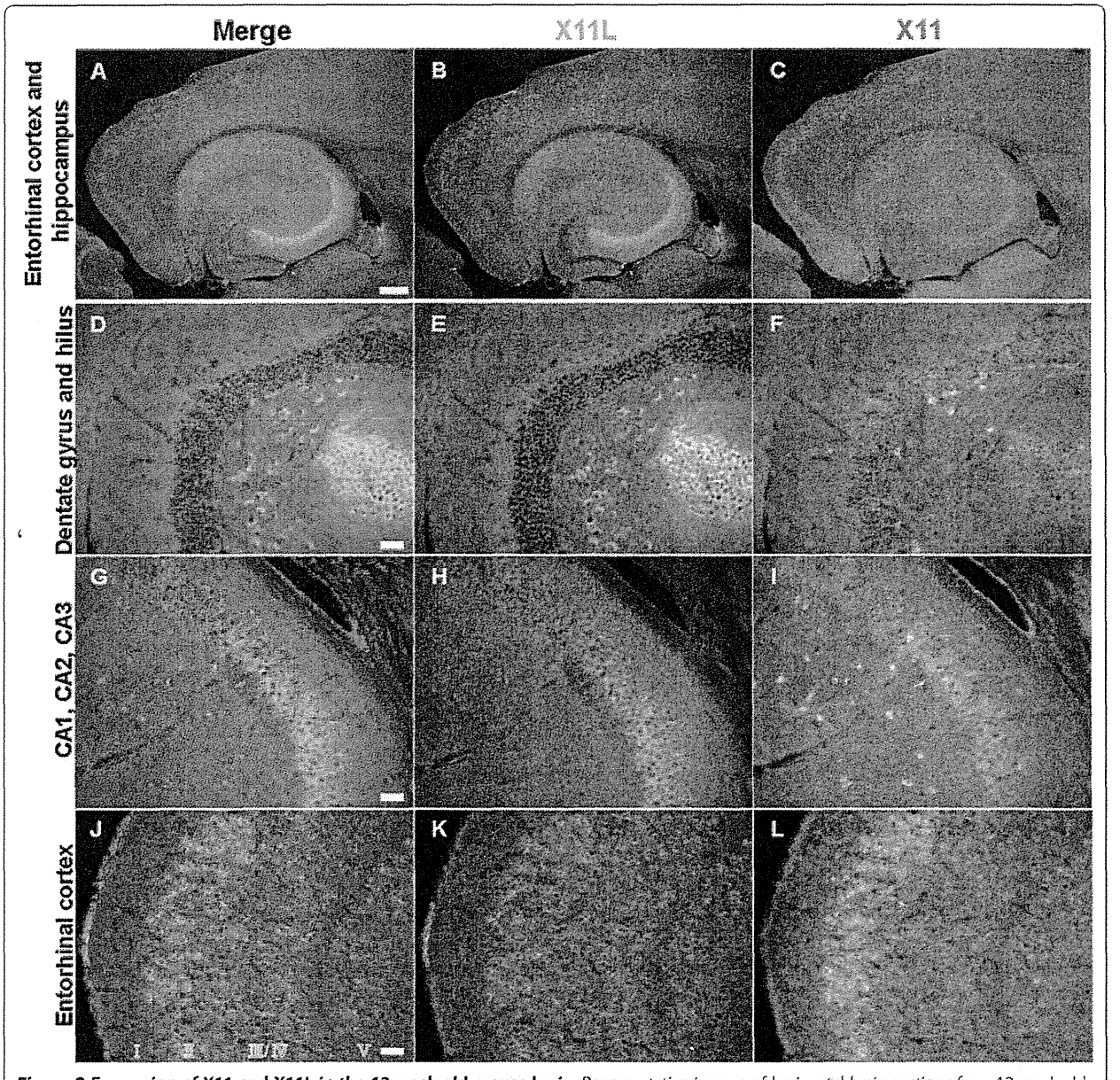

Figure 2 Expression of X11 and X11L in the 13-week-old mouse brain. Representative images of horizontal brain sections from 13-week-old $X11^{+/+}/X11L^{+/+}$ mice were stained for X11 (***C, F, I, L***) and X11L (***B, E, H, K***). Immunohistochemistry was performed with anti-X11 polyclonal rabbit IgG followed by donkey anti-mouse IgG conjugated to Alexa Fluor 488, and anti-X11L monoclonal mouse IgG followed by donkey anti-rabbit IgG conjugated to Cy3. Merged images are shown in the *left panels* (***A, D, G, J***). Blue signals indicate nuclei counter-stained with DAPI. Scale bars, 300 μm (***A–C***), 50 μm (***D–L***).

cause the enhanced expression of c-Fos and Egr-1/Zif268. Thus, a deficiency in both X11 and X11L may cause abnormal, seizure-associated neuronal activity and subsequent alterations in protein expression in the hippocampal formation.

Reduction of Ih currents in entorhinal cortex (EC) layer II of $X11^{-/-}/X11L^{-/-}$ mice

Spontaneous epileptic seizures were observed in mice when both X11 and X11L genes were deficient (Figure 1A, Additional file 1: Figure S1 and additional movies). Because the DG granule cells of $X11^{-/-}/X11L^{-/-}$ mice showed augmented expression of c-Fos and Egr-1/Zif268 following seizure activity, we next performed a detailed examination of the expression of both proteins in hippocampal neurons in 13-week-old murine brains (Figure 2).

Distinct expression patterns of X11 and X11L were observed in the hippocampus of wild type mice. X11L was expressed mainly in the pyramidal neurons of the CA1–3 region (Figure 2B, E, H), whereas X11 was expressed in other types of interneurons (Figure 2C, F, I). These observations coincide with our previous report of X11s expression in aged wild type mice [21]. Unlike c-Fos and Egr-1/Zif268 in the double mutant mouse, X11 and X11L were not expressed in DG granule cells (Figure 2D–F). However, both X11 and X11L were strongly co-expressed in EC layer II (Figure 2J–L), which projects axons primarily to the granule cells of the DG [24]. Furthermore, both HCN1 and HCN2 are expressed in EC layer II [25]. Given that $HCN1^{-/-}$ mice show enhanced seizure susceptibility and that $HCN2^{-/-}$ mice suffer from absence seizures [26,27], we next focused our investigations on the alteration of Ih currents associated with HCN channels in EC layer II in $X11^{-/-}/X11L^{-/-}$ mice.

Horizontal brain slices that included the EC and the hippocampus were prepared from 12–14-week-old $X11^{+/+}/X11L^{+/+}$, $X11^{+/+}/X11L^{-/-}$, $X11^{-/-}/X11L^{+/+}$, and $X11^{-/-}/X11L^{-/-}$ mice. EC layer II neurons were then subjected to electrophysiological analysis, and Ih currents from HCN channels were recorded (Figure 3 and Additional file 1: Figure S2). The mice used in the electrophysiological study were seizure-naïve, at least without over behavioral manifestations, and showed comparable levels of HCN1 channels in the EC (Additional file 1: Figure S3). Similar to a previous report [28], hyperpolarizing voltage steps activated a large Ih current in EC layer II cells of $X11^{+/+}/X11L^{+/+}$ mice (Figure 3A and C). By contrast, the Ih current was dramatically reduced in $X11^{-/-}/X11L^{-/-}$ mice relative to that in $X11^{+/+}/X11L^{+/+}$ mice (Figure 3B and D); however, no significant alterations were observed for the V1/2 (mean ± SEM, $X11^{+/+}/X11L^{+/+}$: −81.1±1.1 mV; $X11^{-/-}/X11L^{+/+}$: −80.3±1.3 mV; $X11^{+/+}/X11L^{-/-}$: −83.5±1.4 mV; $X11^{-/-}/X11L^{-/-}$: −81.3±0.9 mV) (Figure 3E) or the series resistance (mean ± SEM, $X11^{+/+}/X11L^{+/+}$: 8.3±0.2 MΩ; $X11^{-/-}/X11L^{+/+}$: 8.9±0.5 MΩ; $X11^{+/+}/X11L^{-/-}$: 9.2±0.4 MΩ; $X11^{-/-}/X11L^{-/-}$: 8.0±0.2 MΩ) (Figure 3F). Quantitative analysis (Figure 3G) revealed that the density of the Ih current was also significantly reduced in $X11^{-/-}/X11L^{-/-}$ mice (1.12±0.15 pA/pF, n = 9; $p < 0.01$) compared with that in $X11^{+/+}/X11L^{+/+}$ mice (2.18±0.27 pA/pF, n = 10), but did not change significantly in $X11^{-/-}/X11L^{+/+}$ mice (2.41±0.25 pA/pF, n = 9, $p > 0.05$) or in $X11^{+/+}/X11L^{-/-}$ mice (2.05±0.29 pA/pF, n = 9, $p > 0.05$). Thus, genetic ablation of X11 and X11L together had a profound impact on the Ih current in the EC layer II of the double knockout mice. These results correlate with the observation that $X11^{-/-}/X11L^{-/-}$ mice, but not $X11^{+/+}/X11L^{+/+}$, $X11^{+/+}/X11L^{-/-}$, or $X11^{-/-}/X11L^{+/+}$ mice, are susceptible to spontaneous epileptic seizures.

In EC layer II, the dominant HCN subtype is HCN1 [28]. We found that HCN1, X11, and X11L were colocalized in EC layer II neurons (Figure 3H) and apparently formed a complex in the brain (Figure 3I–K). The colocalization of these molecules was observed in a region surrounding the neuronal nucleus (Figure 3H), consistent with the location of the Golgi apparatus. Because X11 and X11L are largely localized in the Golgi apparatus and function in the trafficking of membrane proteins [29,30], the deletion of X11 and X11L may disturb intracellular localization of HCN channels (Additional file 1: Figure S4). While the localization of the channel likely affects its function, we cannot rule out the possibility that X11 and X11L directly regulate HCN1 function as well.

Enhanced Aβ generation according to HCN1 dysfunction

The EC is one of the most vulnerable brain regions in AD [31], and it is well-known that synaptic activity such as that mediated by HCN channels can regulate Aβ generation [8-10]. Therefore, we examined whether HCN channel impairment involved in the aberrant production of Aβ. We first quantified the levels of endogenous Aβ40 and Aβ42 in $HCN1^{-/-}$ mouse brains. Aβ40 and Aβ42 were both significantly increased in the cortex of $HCN1^{-/-}$ mice compared with $HCN1^{+/+}$ mice (average ± SEM, Aβ40: n = 5, $p = 0.0037$; Aβ42: n = 5, $p = 0.0055$) (Figure 4A). The magnitude of the increase in Aβ40 and Aβ42 was inversely proportional to the level of HCN1 gene expression (Figure 4A, left panel), while APP protein levels were comparable in $HCN1^{+/+}$, $HCN1^{+/-}$, and $HCN1^{-/-}$ mice (Figure 4A, right panel).

To confirm whether the increase in Aβ generation in $HCN1^{-/-}$ mice depends on the decrease in HCN channel activity, we used N2a cells that transiently overexpressed FLAG-APP and HCN1 (Figure 4B). Overexpression of HCN1 significantly reduced the generation of Aβ40 and Aβ42 (compare column 2 with column 3 for each Aβ peptide). The Aβ levels were restored by adding ZD7288, a

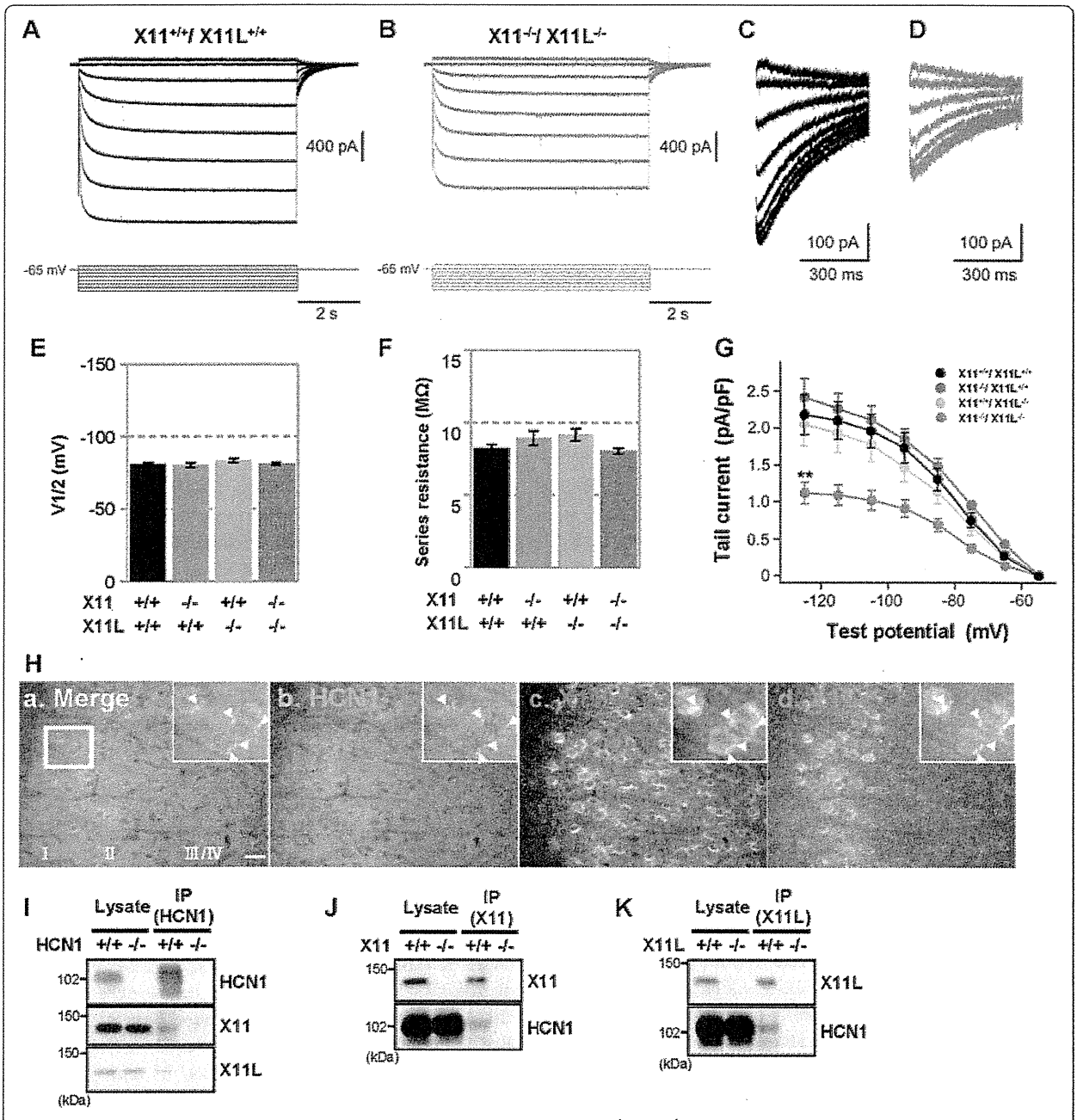

Figure 3 Reduction of Ih currents in entorhinal cortex layer II neurons of $X11^{-/-}/X11L^{-/-}$ mice. (*A, B*) Representative electrophysiological recordings of Ih currents from EC layer II neurons in $X11^{+/+}/X11L^{+/+}$ (*A*) and $X11^{-/-}/X11L^{-/-}$ (*B*) mice. (*C, D*) Tail currents of $X11^{+/+}/X11L^{+/+}$ (*C*) and $X11^{-/-}/X11L^{-/-}$ (*D*) mice. (*E*) Quantitative data of the voltage, whereby the current is half-activated (V1/2). Statistical analysis was performed using one-way analysis of variance followed by Tukey's multiple comparison test (mean ± SEM (mV); five slices from two $X11^{+/+}/X11L^{+/+}$ mice, n = 10; four slices from two $X11^{-/-}/X11L^{+/+}$, $X11^{+/+}/X11L^{-/-}$, and $X11^{-/-}/X11L^{-/-}$ mice, n = 9). (*F*) Quantitative data of series resistance. Statistical analysis was performed as described (mean ± SEM (MΩ); five slices from two $X11^{+/+}/X11L^{+/+}$ mice, n = 10; four slices from two $X11^{-/-}/X11L^{+/+}$, $X11^{+/+}/X11L^{-/-}$, and $X11^{-/-}/X11L^{-/-}$ mice, n = 9). (*G*) Summary of the current density of the tail currents. Statistical analysis was performed as described (mean ± SEM (pA/pF); five slices from two $X11^{+/+}/X11L^{+/+}$ mice, n = 10; four slices from two $X11^{-/-}/X11L^{+/+}$, $X11^{+/+}/X11L^{-/-}$, and $X11^{-/-}/X11L^{-/-}$ mice, n = 9; $^{**}p < 0.01$). (*H*) Representative images of the HCN1-X11-X11L complex in EC layer II neurons of 13-week-old $X11^{+/+}/X11L^{+/+}$ mice (a, merge; b HCN1 (green); c, X11L (red); d, X11(blue)). Scale bar, 20 μm. (*I–K*) Co-immunoprecipitation of HCN1-X11s complexes from the 13-week-old $X11^{+/+}/X11L^{+/+}$ murine cortex. $HCN1^{-/-}$ (*I*), $X11^{-/-}$ (*J*), or $X11L^{-/-}$ (*K*) mice were used as controls. Brain lysates were immunoprecipitated with anti-HCN1 (*I*), anti-X11 (*J*), and anti-X11L/Mint2 (*K*) antibodies. Immunocomplexes were detected by immunoblotting.

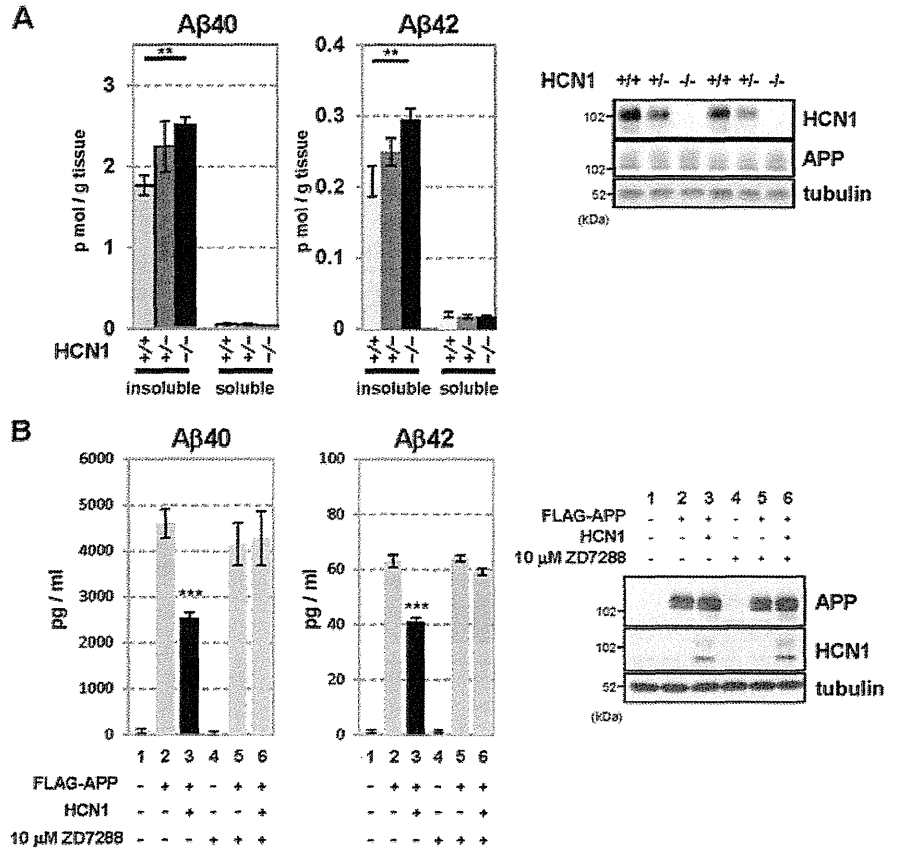

Figure 4 Functional deficits in the HCN1 channel facilitate Aβ generation. (*A*) Quantification of endogenous murine Aβ40 and Aβ42 in the cortex of 4-month-old HCN1$^{+/+}$, HCN1$^{+/-}$, and HCN1$^{-/-}$ mice by using the sELISA system (left panels). Statistical analysis was performed using the two-tailed Mann–Whitney *U*-test (average ± SEM, n = 5, **p < 0.01). (*B*) Quantification of Aβ40 and Aβ42 secreted into the culture medium by N2a cells by using the sELISA system. FLAG-APP or FLAG-APP and HCN1 were transiently overexpressed in the cells with (+) or without (–) 10 μM ZD7288 (left panels). Statistical analysis was performed using one-way analysis of variance followed by Tukey's multiple comparison test (average ± SEM, n = 4, ***p < 0.001). Expression levels of APP and HCN1 was confirmed by immunoblotting (right panels in *A* and *B*).

selective inhibitor of HCN channel activity (compare lanes 3 through 6). Although we have not confirmed the blockage of channel activity electrophysiologically, ZD7288 had no effect on Aβ levels in cells without HCN1 expression (column 5), and APP expression was not affected by either the presence of HCN1 or by the administration of ZD7288 (Figure 4B, right panel). Furthermore, administration of ZD7288 did not influence the interaction of HCN1 with APP (Additional file 1: Figure S5). These results suggest that the suppression of Aβ generation in HCN1-overexpressing cells probably depends on channel activity (Figure 4B), in agreement with the *in vivo* observation that the brains of mice lacking the HCN1 gene and with impaired HCN channel activity (Figure 3B, D, and G) demonstrated increased Aβ generation (Figure 4A).

Association of HCN1 with APP *in vivo* and *in vitro*

Increased synaptic activity enhances Aβ generation [8-10], and modulation of Aβ generation is not limited to alterations in HCN1 channel activity. Indeed, APP metabolism is thought to be largely regulated by APP-binding partners [14]. Therefore, we next explored the hypothesis that HCN1 might be involved in regulating APP metabolism via a physical interaction between the channel and APP. In support of this hypothesis, an anti-HCN1 antibody co-immunoprecipitated APP together with HCN1 from a lysate of wild type murine cortex (Figure 5A). The interaction seemed to be specific in that APP was not recovered from the cortical lysate of HCN1$^{-/-}$ mice. The association between APP and HCN1 was next confirmed in the EC. Using EC-rich brain samples isolated from HCN1$^{+/+}$ and HCN1$^{-/-}$ mice (Additional file 1: Figure S3A), a co-immunoprecipitation assay was performed with an anti-HCN1 antibody, and the immunoprecipitates were analyzed with the indicated antibodies (Figure 5B). Along with X11 and X11L, APP was co-immunoprecipitated with HCN1 in EC-rich brain samples of wild type mice (Figure 5B), suggesting that HCN1 can complex with

APP and X11/X11L *in vivo*. These results are in agreement with the co-localization results of HCN1, X11, and X11L in the wild type cortex shown above (Figure 3H–K). Tubulin and PSD95 (postsynaptic density protein 95) were not detected in the immunocomplex, indicating the specific association of APP and X11/X11L with HCN1.

To show whether HCN1 directly binds to APP without mediation by X11/X11L, FLAG-APP and HCN1 were transiently expressed in N2a cells and a co-immunoprecipitation

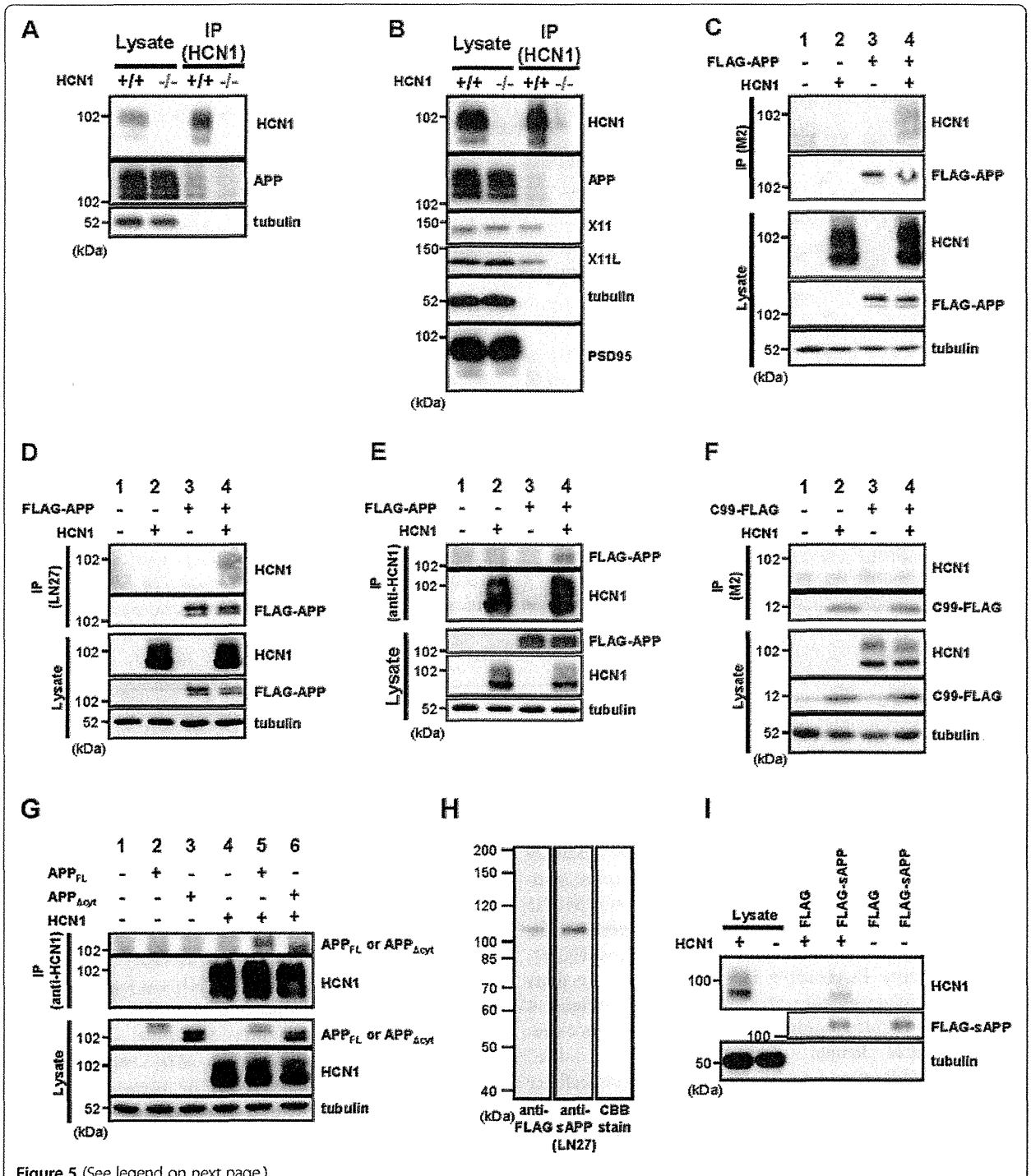

Figure 5 (See legend on next page.)

(See figure on previous page.)
Figure 5 APP and HCN1 form a molecular complex *in vivo* and *in vitro*. (***A***) Co-immunoprecipitation of the HCN1-APP complex from the wild type and HCN1$^{-/-}$murine cortex. Brain lysates were immunoprecipitated with an anti-HCN1 antibody. Immunocomplexes were detected by immunoblotting. (***B***) Co-immunoprecipitation of HCN1-APP, -X11 and -X11L complexes from the EC-rich cortex (see Additional file 1: Figure S2). Brain lysates were immunoprecipitated with an anti-HCN1 antibody. Immunocomplexes were detected by immunoblotting. (***C–G***) Co-immunoprecipitation of the HCN1-APP complex from N2a cells transiently overexpressing FLAG-APP and murine HCN1. (***C–E***), Analysis of FLAG-APP and murine HCN1, (***F***) C99-FLAG and murine HCN1, and (***G***) APP_{FL} or $APP_{\Delta cyt}$ and murine HCN1 immunocomplexes. To standardize the amount of plasmid, empty vector (–) was added to yield 1.2 μg of plasmid in total. Cell lysates were immunoprecipitated with anti-FLAG M2 (*C* and *F*), anti-APP extracellular domain (LN27) (*D*), or anti-HCN1 (***E*** and ***G***) antibodies. Immunocomplexes were detected by immunoblotting. (***H***) Affinity purification of FLAG-sAPP secreted into the culture medium by N2a cells expressing FLAG-APP. The purification was performed using anti-FLAG M2 affinity beads. FLAG-sAPP were specifically detected by M2 and anti-APP extracellular domain (LN27) antibodies, and no contaminating bands were identified by CBB-staining. (***I***) Pull-down of HCN1 with affinity purified FLAG-sAPP prepared in (H). Lysates from wild type cells (–) and cells that transiently expressed HCN1 (+) were incubated with M2 affinity beads coupled with FLAG-tag or FLAG-sAPP. The complexes resulting from the pull-down assay were subjected to immunoblot analysis with anti-HCN1 antibody.

assay was performed. The anti-FLAG M2 antibody immunoprecipitated HCN1 along with FLAG-APP (Figure 5C). An anti-hAPP extracellular domain antibody (LN27) also recovered HCN1 (Figure 5D), and anti-HCN1 antibody recovered FLAG-APP (Figure 5E).

APP is a type I transmembrane protein composed of a large extracellular (luminal) domain of 596 amino acids and a small intracellular domain of 47 amino acids. On the other hand, HCN1 is six-transmembrane protein with short extracellular sequences between transmembrane regions one and two, three and four, and five and six; and long intracellular domains within the amino- and carboxyl-terminal regions of the protein. To determine the region of APP that binds to HCN1, we performed co-immunoprecipitation assays using APP deletion mutants (C99-FLAG, which largely lacks the extracellular domain of APP and in which FLAG is fused to the carboxyl terminal region of APP; and $APP_{\Delta cyt}$, which lacks the 43- amino acid carboxyl terminal region of APP) (Figure 5F, G). The results of this assay indicated that HCN1 was not co-immunoprecipitated with C99-FLAG (Figure 5F), whereas $APP_{\Delta cyt}$ was co-immunoprecipitated with HCN1 (Figure 5G).

Next, we performed an *in vitro* pull-down assay with FLAG-soluble APP (FLAG-sAPP, consisting of the extracellular domain of APP cleaved at the α- and/or β-cleavage sites). FLAG-sAPP was purified with affinity beads (anti-FLAG M2 affinity gel) from the culture medium of N2a cells expressing FLAG-APP (Figure 5H) and then incubated with lysates of N2a cells that expressed HCN1. HCN1 bound to FLAG-sAPP, but not to FLAG-tag alone (Figure 5I). Taken together, the results shown in Figure 5 indicate that HCN1 associates with APP through its extracellular (luminal) domain.

Hence, HCN1 apparently interacts with the extracellular domain of APP (Figure 5) and with both X11 and X11L in the cytoplasm (Figure 3H–K, Figure 5B). This suggests that the HCN1 channel might form a ternary complex with APP and either X11 or X11L to regulate Aβ generation. However, the detailed molecular regulation of complex formation remains to be determined.

Age- and AD state-dependent HCN disruption in the temporal cortex (superior temporal gyrus) of cynomolgus monkeys and sporadic AD patients

Advanced age is the greatest risk factor for AD. To examine the relationship between aging and HCN1 levels, we quantified the amount of HCN1, Aβ, APP, and actin in freshly frozen brain tissues (superior temporal gyrus) from cynomolgus monkeys of various ages (Figure 6A and Additional file 1: Figure S6). Senile plaques and neurofibrillary tangles spontaneously appear in the brains of cynomolgus monkeys with advancing age [32,33], and the amino acid sequence of Aβ in cynomolgus monkeys is identical to that in humans [34]. Thus, we hypothesized that the cynomolgus monkey would be a useful animal model for the investigating the relationship between aging and AD pathology. Significant negative correlations were found between HCN1 levels and age ($n = 39$, $r = -0.5363$, $p = 0.0004$) (Figure 6A, left), between HCN1 and APP levels ($n = 39$, $r = -0.3796$, $p = 0.0086$) (Additional file 1: Figure S6B), between HCN1 and TBS-insoluble Aβ40 levels ($n = 39$, $r = -0.2878$, $p = 0.0421$) (Additional file 1: Figure S6C and D), and between HCN1 and Tris buffered saline (TBS)-insoluble Aβ42 levels ($n = 39$, $r = -0.2913$, $p = 0.0401$) (Additional file 1: Figure S6E and F). A significant positive correlation was found between age and APP level ($n = 39$, $r = 0.8156$, $p < 0.0001$) (Additional file 1: Figure S6A), and a significant weak-positive correlation was found between APP and TBS-insoluble Aβ42 levels ($n = 39$, $r = 0.3714$, $p = 0.0236$) (Additional file 1: Figure S6H). However, no correlation was found between age and actin level ($n = 39$, $r = -0.1981$, $p = 0.2266$) (Figure 6A, right) or between APP and TBS-insoluble Aβ40 levels ($n = 39$, $r = 0.2993$, $p = 0.072$) (Additional file 1: Figure S6G).

Finally, we examined the possibility of altered HCN1 levels in human AD brain specimens obtained at autopsy

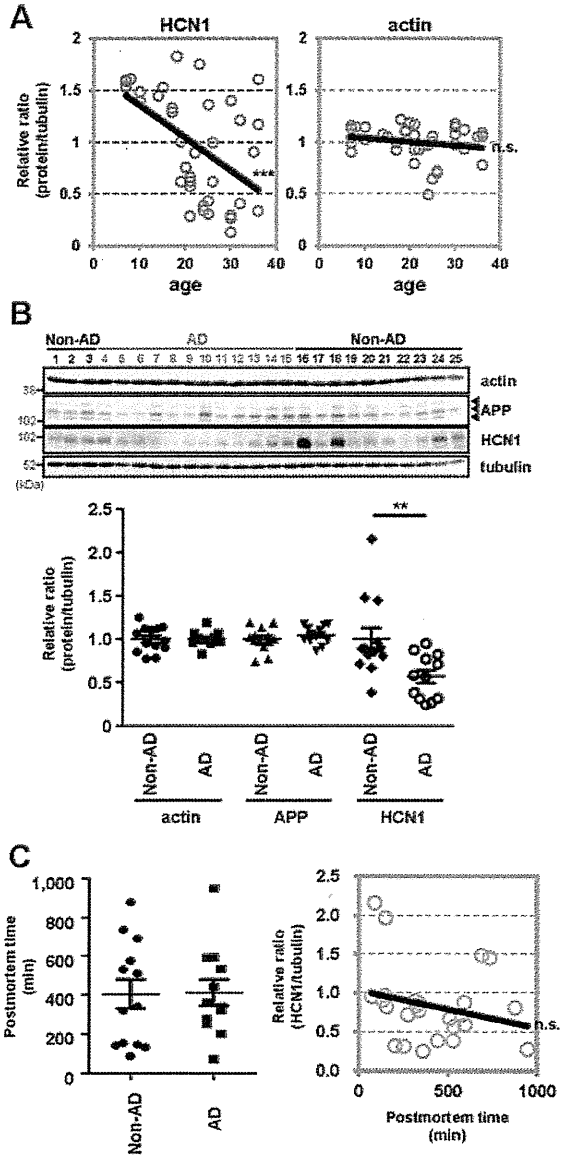

Figure 6 HCN1 levels decrease in a age- and AD-dependent manner. (*A*) Quantification of the amount of HCN1 and actin in the brain (superior temporal gyrus) of 4–37-year-old cynomolgus monkeys by immunoblotting. Statistical analysis was performed using the two-tailed Pearson's correlation coefficient (HCN1: n = 39, r = −0.5363, ***p < 0.001; actin: n = 39, r = −0.1981, p > 0.05). (*B*) Quantification of the amount of HCN1, APP, actin, and tubulin in age-matched AD and non-AD postmortem brains (superior temporal gyrus) by immunoblotting. Statistical analysis was performed using the two-tailed Mann–Whitney *U*-test (non-AD: n = 13, AD: n = 12, **p < 0.01). (*C*) Comparison of postmortem time between non-AD and AD samples. Statistical analysis was performed using the two-tailed Mann–Whitney *U*-test (non-AD: n = 13, AD: n = 12, p = 0.8066). The correlation between postmortem time and HCN1 level was analyzed. Statistical analysis was performed using the two-tailed Pearson's correlation coefficient (n = 39, r = −0.2416, p = 0.2446). Descriptions of all subjects are provided in Table 1.

(Figure 6B and Table 1). The postmortem time was not significantly different for the AD and non-AD brain samples used in this study (non-AD: n = 13, AD: n = 12, p = 0.8066), and no significant decrease in HCN1 levels related to postmortem time was observed (n = 25, r = −0.2416, p = 0.2446) (Figure 6C and Table 1). Of great relevance to this study, the amount of HCN1 was significantly reduced in AD brains (superior temporal gyrus) compared with that in age-matched control brains (non-AD: n = 13, AD: n = 12, p = 0.0083), while the levels of APP and actin were not significantly altered (Figure 6B and Table 1). These results suggest that the reduction in HCN1 expression that occurs with age (Figure 6A) may be involved in the aggravation of the pathology of AD.

Discussion

X11 and X11L are well-characterized neural adaptor proteins that regulate the trafficking and metabolism of APP [14]. Many reports indicate that X11s bind to APP and suppress Aβ generation *in vitro* and *in vivo* [14-22]. Furthermore, X11s are thought to mediate a number of cellular functions through their association with various proteins [35]. This report showed that mutant mice lacking both X11 and X11L present with dysfunctional HCN1 channel activity and epileptic seizures. Notably, AD patients are also at increased risk of epileptic seizures. Furthermore, mutant mice lacking HCN1 demonstrated increased generation of Aβ, which is a causative factor for the development of AD.

The incidence of AD dramatically increases with age. We found that the amount of HCN1 decreased with both aging and in AD. The dysfunction of HCN1 that occurs over time may, thus, be a trigger for epileptic seizures and the pathogenic generation of Aβ in AD.

Several converging studies corroborate the premise that HCN channel activity is closely related to epileptogenesis [11]. For example, HCN1 expression is significantly reduced in the EC after temporal lobe epilepsy [36,37]. Furthermore, HCN1 channel plasticity in cortical neurons is similar in multiple epileptic animal models [38-43]. Moreover, kainic acid-induced seizure susceptibility is increased in HCN1$^{-/-}$ mice [27], and HCN2-deficient mice exhibit spontaneous absence seizures [26].

HCN1$^{-/-}$ mice show a significantly higher number of negative resting membrane potentials and a significantly higher input resistance measured from responses to either negative or positive current steps [28]. As such, seizure susceptibility is increased in HCN1$^{-/-}$ mice [27], indicating that loss of the HCN1 subunit enhances neuronal excitability, which can increase Aβ generation [8-10]. These observations suggest that enhanced Aβ generation in HCN1$^{-/-}$ mice results from neuronal hyper-excitability, which is in turn caused by ablation of the HCN1 gene.

Table 1 Summary of subject information presented in Figure 6B and C

Sample no.	Subject	Age	Sex	Post mortem time (min)	Braak stage	Seizure	Relative ratio (protein/tubulin)		
							Actin	APP	HCN1
1	Normal	84	F	877	1	-	0.929	1.192	0.809
2	Normal	88	F	144	1	-	0.856	1.046	0.859
3	Normal	70	M	340	0.5	-	0.955	1.189	0.859
4	AD	84	M	71	4	-	0.950	1.171	0.952
5	AD	70	M	276	4	-	0.829	0.986	0.716
6	AD	74	M	322	5	-	0.961	0.990	0.827
7	AD	75	M	594	6	-	1.069	1.176	0.589
8	AD	76	M	947	6	+	1.190	1.167	0.273
9	AD	79	F	203	5	-	1.019	0.913	0.317
10	AD	81	M	360	6	-	0.971	0.862	0.247
11	AD	81	F	442	5	-	0.971	0.862	0.385
12	AD	82	F	254	6	-	0.988	1.029	0.313
13	AD	82	F	533	5	-	0.988	1.001	0.566
14	AD	82	F	338	4	-	1.028	1.063	0.770
15	AD	84	M	590	5	-	1.071	1.128	0.876
16	Normal	78	F	87	2	-	1.108	1.138	2.153
17	Normal	81	M	134	1	-	1.122	0.971	0.902
18	Normal	82	F	148	1	-	1.178	1.109	1.963
19	Normal	82	F	155	2	-	1.141	1.026	0.821
20	Normal	80	M	317	2	-	1.254	1.037	0.893
21	Normal	80	M	510	2	-	1.071	0.778	0.669
22	Normal	82	M	530	1	-	0.979	0.916	0.384
23	Normal	78	M	575	1	-	0.905	1.007	0.713
24	Normal	78	M	690	1	-	0.784	0.986	1.479
25	Normal	82	M	736	1	-	0.774	0.743	1.448

Postmortem brain samples were obtained from the Brain Bank for Aging Research, Tokyo Metropolitan Institute of Gerontology. Experimental procedures were approved by the appropriate ethical boards at each institute. Autopsies were performed with written informed consent from the patients or their relatives. The clinical diagnosis of AD was based on two major criteria: the Diagnostic and Statistical Manual of Mental Disorders: 4th Edition (DSM-IV) and the National Institute of Neurological and Communicational Disorders and Stroke-Alzheimer's Disease and Related Disorders Association (NINCDS-ADRDA). The neuropathological diagnosis of AD was made using Consortium to Establish a Registry for Alzheimer's Disease criteria (average age at death, 79.2 ± 4.4 years). Control brains were obtained from age-matched individuals with no history of neurological or psychiatric illness (average age at death, 80.4 ± 4.2 years). Subjects, age, gender, postmortem time, Braak stage, seizure history, and relative protein/tubulin ratios are indicated.

On the other hand, the present study showed that HCN1 physically associated with APP through the extracellular domain of APP. Therefore, HCN1-mediated regulation of Aβ generation may depend on a molecular linkage between HCN1 and APP and not simply on alterations in neuronal excitability. However, the molecular mechanism by which HCN1 potentially links epileptic seizures to Aβ generation in AD remains to be elucidated.

Our results suggest that ablation of X11/X11L induces aberrant HCN1 distribution and function along with epilepsy. Although the molecular mechanism by which X11s regulates HCN channel activity also remains unclear, X11s are known to modulate intracellular trafficking of membrane proteins. For example, X11s interact with certain proteins implicated in traffic and transport, such as Arfs, Rab6, and KIF17 [29,44,45]. Furthermore, X11s bind to vesicular cargo proteins, such as APP and alcadein [16,46,47] and regulate the intracellular distribution of APP [21,30]. We hypothesize that X11 and X11L similarly influence the trafficking and/or intracellular localization of HCN1. We further hypothesize that the mislocalization of HCN1 observed in $X11^{-/-}$/$X11L^{-/-}$ mice (Additional file 1: Figure S4) may cause aberrant excitatory neuronal activities, resulting in epileptic seizures.

In conclusion, this study indicates that HCN1 may play an important role in the regulation of neuronal

activity, along with Aβ generation in the hippocampal formation. However, we cannot rule out the possibility that additional ion channels (e.g., M-channels, Kir-channels, and sodium leak channels) also participate in the regulation of APP metabolism. Taken together, the current observations may provide new insights into the mechanisms underlying the linkage between epileptic seizures and Aβ generation in AD.

Methods

Animals and human non-AD and AD brain samples

All animal studies were conducted in compliance with the guidelines of the Animal Studies Committees of Hokkaido University (Sapporo, Japan), Shiga University (Shiga, Japan), and the National Institute of Biomedical Innovation (Osaka, Japan). Mice were maintained under a 12-h light/12-h dark cycle (lights on, 7:00 A.M.–7:00 P.M.), and provided with food and water *ad libitum*. $X11^{-/-}/X11L^{+/+}$, $X11^{+/+}/X11L^{-/-}$, and $X11^{-/-}/X11L^{-/-}$ mice have already been described [20,21]. $HCN^{-/-}$ mice (stock number 005034) were purchased from The Jackson Laboratory (Bar Harbor, Maine). Male mice were used for all experiments.

Brain samples containing the superior temporal gyrus of cynomolgus monkeys (*Macaca fascicularis*) were obtained from Shiga University of Medical Science and the National Institute of Biomedical Innovation. The monkeys were housed in individual cages prior to the experiment and were maintained according to institutional guidelines for experimental animal welfare. Human brain samples containing the superior temporal gyrus (Broadmann area 22) were obtained from the Brain Bank for Aging Research, the Tokyo Metropolitan Institute of Gerontology (Itabashi, Tokyo, Japan). Human temporal cortical specimens for the quantification of proteins were obtained from brains that were removed, processed, and stored at −80°C within 16 h postmortem at the Brain Bank at Tokyo Metropolitan Institute of Gerontology. (Patients were placed in a cold (4°C) room within 2 h of death.) For all brains registered at the bank, written informed consent for their use for medical research was obtained from the patient prior to death or from the patient's family. Brain specimens were collected from Broadmann area 22 (superior temporal gyrus) for 12 AD patients (79.2±4.4 years of age) and 13 control patients (80.4±4.2 years of age) [48]. Detailed descriptions of all subjects, including the relative protein/tubulin ratio for each individual, are shown in Table 1.

Antibodies

Polyclonal rabbit anti-HCN1 antibody [25] and polyclonal rabbit anti-X11 UT153 antibody [21] have already been described. Monoclonal mouse anti-tubulin DM1A antibody and polyclonal rabbit anti-c-Fos, rabbit anti-Egr-1, and goat anti-HCN1 antibodies (sc-19706) were purchased from Santa Cruz Biotechnology (Santa Cruz, CA, USA). Characterization and demonstration of the antigen-specificity of the goat anti-HCN1 antibody (sc-19706) is shown in Additional file 1: Figure S7. Monoclonal mouse anti-X11L/mint2 and anti-PSD95 antibodies were purchased from BD Transduction Laboratories (Lexington, KY, USA). Anti-actin antibody and the anti-HCN1 antibody, AB5884, were purchased from Millipore (Billerica, MA, USA). Anti-FLAG M2 and polyclonal rabbit anti-APP cytoplasmic domain (N-terminus) antibodies were purchased from Sigma-Aldrich (St. Louis, MO, USA), and the anti-human APP extracellular domain antibody (LN27) was purchased from Zymed (San Francisco, CA, USA). Anti-FLAG M2 affinity gel and FLAG peptide were purchased from Sigma-Aldrich.

Plasmid construction

Human APP695 (hAPP695) and FLAG-APP695 cDNA were inserted into the pcDNA3 plasmid at the HindIII/XbaI restriction sites to produce pcDNA3-hAPP695 and pcDNA3-FLAG-hAPP695 [46]. The cDNA constructs pcDNA3-$hAPP_{\Delta cyt}$ (in which amino acids 652–695 of hAPP695 are deleted) and pcDNA3.1-C99-FLAG (in which the signal sequence of hAPP is inserted into the 5' region of C99) were generated by PCR using pcDNA3-hAPP695 as the template. The generated fragments were ligated into pcDNA3-hAPP695 and pcDNA3.1-FLAG at the BamHI/XbaI restriction site and the HindIII/XbaI restriction site, respectively. The pCI-*murine* HCN1 vector was a kind gift from Dr. Takahiro M. Ishii [49].

Immunohistochemistry

Murine brain tissue sections were prepared and incubated with primary antibodies as described [21]. The sections were further incubated with goat anti-rabbit IgG antibodies conjugated to biotin (Vector Laboratories, Burlingame, CA, USA), followed by the ABC complex. Peroxidase activity was revealed using diaminobenzidine as the chromogen. Alternatively, sections were incubated with donkey anti-mouse IgG coupled with Alexa Fluor 488, donkey anti-rabbit IgG coupled with Cy3, or donkey anti-goat IgG coupled with Alexa Fluor 633 in phosphate buffered saline (PBS) containing 3% bovine serum albumin (BSA) for 2 h at room temperature. Sections were mounted onto slides with Shandon Immu-Mount (Thermo, Pittsburgh, PA, USA) and viewed under a BZ-9000 microscope (Keyence, Woodcliff Lake, NJ, USA).

Immunoblotting and co-immunoprecipitation analysis

The cortices of wild type, $X11^{-/-}/X11L^{+/+}$, $X11^{+/+}/X11L^{-/-}$, $X11^{-/-}/X11L^{-/-}$, $HCN1^{+/-}$, and $HCN1^{-/-}$ mice, and cynomolgus monkey brains (superior temporal gyrus) and human post-mortem brains (superior temporal gyrus) were homogenized in eight volumes of radioimmune

precipitation assay buffer containing 0.5% (w/v) sodium dodecyl sulfate (SDS) and a protease inhibitor mixture (5 μg/ml chymostatin, 5 μg/ml leupeptin, and 5 μg/ml pepstatin). The homogenates were lysed by sonication on ice and centrifuged at 20,000 × g for 10 min at 4°C. The resulting supernatants were used for immunoblot analysis. Proteins (10 μg per lysate) were separated via SDS (w/v) polyacrylamide gel electrophoresis (SDS-PAGE) on 7.5% (w/v) polyacrylamide gels.

The cortex (from one mouse) and EC-rich region (from five mice) from wild type and gene-null mice were homogenized in eight volumes of HBS-T lysis buffer (10 mM HEPES [pH 7.6] containing 150 mM NaCl, 5 mM EDTA, 0.5% [v/v] Triton X-100, 5 μg/ml chymostatin, 5 μg/ml leupeptin, and 5 μg/ml pepstatin A). Homogenates were then centrifuged at 20,000 × g for 10 min at 4°C. N2a cells (~1 × 10^6) were transiently transfected with 0.8 μg pcDNA3-FLAG-hAPP695, pcDNA3-hAPP695, pcDNA3-hAPP$_{\Delta cyt}$, or pcDNA3.1-C99-FLAG and 0.4 μg of pCI-*murine* HCN1 using Lipofectamine 2000 (Invitrogen) and cultured for 24 h in medium (DMEM) containing 10% (v/v) fetal bovine serum (FBS). Cells were harvested, lysed in lysis buffer (PBS containing 1.0% [v/v] Triton X-100, 5 μg/ml chymostatin, 5 μg/ml leupeptin, and 5 μg/ml pepstatin A), and centrifuged for 5 min at 4°C. The resulting supernatants were incubated with anti-FLAG M2, anti-hAPP extracellular domain (LN27), anti-HCN1, anti-X11, or anti-X11L/Mint2 antibody at 4°C for 2 h. Each immunocomplex was recovered with Dynabeads® Protein G (Invitrogen) and washed three times with lysis buffer. The proteins were separated on 7.5% (w/v) polyacrylamide gels, transferred onto nitrocellulose membranes, and analyzed by immunoblotting with the indicated antibodies. The immunoreactants were detected using the ECL plus™ detection system (GE Healthcare, Houston, TX, USA) and quantified using a Versa Doc model 3000 (Bio-Rad, Hercules, CA, USA).

Affinity purification of FLAG-sAPP from N2a conditioned medium and immunoprecipitation of APP-HCN1 complex

N2a cells (~8.8 × 10^6) were transiently transfected with 5 μg pcDNA3-FLAG-hAPP695 using Lipofectamine 2000 (Invitrogen) and cultured for 24 h in 8 mL of medium (DMEM) containing 10% (v/v) FBS. FLAG-sAPP was collected from the conditioned culture medium by using 50 μL of anti-FLAG M2 affinity gel. The collected FLAG-sAPP that was bound to the gel was washed twice with wash buffer I (20 mM Tris–HCl [pH 8.0], 1 M NaCl, and 0.1% Triton X-100) and twice with wash buffer II (50 mM Tris–HCl [pH8.0], 150 mM NaCl, 1% Triton X-100, 0.05% SDS, and 5 mM EDTA). Collected FLAG-sAPP was then eluted from the affinity gel with 20 μg FLAG-peptide and subjected to immunoblotting and Coomassie brilliant blue (CBB) staining to ascertain the degree of purification.

FLAG-sAPP or FLAG-peptide coupled to anti-FLAG M2 affinity beads were then incubated for 2 h at 4°C with HBS-T-soluble lysates derived from wild type N2a cells or N2a cells transiently overexpressing HCN1. The beads were washed three times with HBS-T lysis buffer. The proteins bound to the beads were separated on 7.5% (w/v) polyacrylamide gels, transferred onto membranes, and analyzed by immunoblotting with the indicated antibodies. The immunoreactants were detected using the ECL plus™ detection system (GE Healthcare) and quantified using a Versa Doc model 3000 (Bio-Rad).

Quantification of Aβ40 and Aβ42

Endogenous murine Aβ was measured as described previously [21] using cortices dissected from 4-month-old mice. Murine Aβ40 and Aβ42 were measured using a sandwich ELISA (sELISA) system (mouse/rat Aβ40 and Aβ42 assay kit, Immuno-Biological Laboratories (IBL), Fujioka, Japan). N2a cells (~2 × 10^5) were transiently transfected with 0.2 μg pcDNA3-FLAG-hAPP695 and 0.1 μg pCI-*murine* HCN1 using Lipofectamine 2000 (Invitrogen) and cultured in medium (DMEM) containing 10% (v/v) FBS. After 24 h, cells were incubated in fresh medium for an additional 4 h with or without 10 μM ZD7288 (Tocris Bioscience, Bristol, UK). Human Aβ40 (hAβ40) and hAβ42 secreted into the culture medium during the 4-h incubation were quantified using the sELISA system.

Electroencephalogram recording

To obtain free-moving cortical electrocorticogram recordings, recording and reference electrodes were screwed onto the skull over the temporal (anterior = −3.1 mm, lateral = 2.5 mm, relative to bregma) and occipital regions of the murine brain. Recordings were continuously made using a cortical electroencephalogram linked to a telemetry system (Unimec, Usmate Velate, Italy) throughout the experiment [50].

Ih current recording

All experiments were performed in a blinded manner. Mice (12–14 weeks old) were anesthetized with halothane (Takeda Chemical Industries) and then sacrificed by decapitation. The brain was rapidly removed and immediately placed in a cold (4°C) cutting solution, which contained 234 mM sucrose, 2.5 mM KCl, 1.1 mM NaH_2PO_4, 10 mM $MgSO_4$, 26 mM $NaHCO_3$, 12 mM glucose, and 0.5 mM $CaCl_2$. Horizontal slices (300 μm thick), which included the EC and the hippocampus, were prepared using a vibratome (VT1000S, Leica, Nussloch, Germany). During recording, individual slices were transferred to a submerged recording chamber and continuously perfused with artificial cerebrospinal fluid (ACSF) maintained at 30–32°C. The ACSF contained 125 mM

NaCl, 2.5 mM KCl, 1.1 mM NaH_2PO_4, 1.0 mM $MgSO_4$, 26 mM $NaHCO_3$, 12 mM glucose, and 2.0 mM $CaCl_2$ and was saturated with 95% O_2 and 5% CO_2. Whole-cell patch-clamp recordings were obtained from principal excitatory cells in layer II of the EC. The patch pipettes were filled with an intracellular solution containing 30 mM K-methanesulfonate, 6 mM NaCl, 0.2 mM EGTA, 10 mM HEPES, 4 mM Mg-ATP, 0.3 mM Na_3-GTP, and 10 mM phosphocreatine-Tris (pH 7.3). In layer II cells of the EC, the hyperpolarization-induced and "slowly-activating" inward currents in the voltage-clamp mode mainly consisted of Ih currents [51]. When Ih currents were studied in the voltage-clamp mode, membrane potentials were first held at −65 mV, and then voltage steps with a duration of 7 s were applied from −55 mV to −125 mV (10 mV increments), after which the holding potentials were allowed to return to −65 mV to obtain the tail currents. The amplitudes of the tail currents at 50 ms after the end of the final voltage step were analyzed to obtain the Ih currents. In all electrophysiological analyses, pooled data were represented as the mean ± SEM.

Statistical analysis

Statistical analyses were performed using a two-tailed Mann–Whitney *U*-test, a one-way analysis of variance followed by Tukey's multiple comparison test, or the two-tailed Pearson's correlation coefficient. All analyses were conducted with GraphPad Prism 5 software.

Additional files

Additional file 1: Figure S1. Simultaneous recording of electrocorticogram in epilepsy model mice and corresponding movie. A representative electrocorticogram recorded during the interictal period in 13-week-old $X11^{-/-}$/ $X11L^{-/-}$ mice (n = 4) is shown. The underlined region indicates the time frame of the corresponding movie (Movie S3). **Figure S2.** Individual data of Ih currents density in entorhinal cortex layer II neurons of wild-type and X11s-null mice. (***A***) Indicidual data of Ih current density. Blue indicate the data of mouse #1 and red indicate mouse #2. (***B***) Mean, SD, SEM, and count number of *A*. P Value of Student's t-test (#1 vs #2) shown in bottom line. (***C***) Distribution and average of current density of *A*. Closed symbols indicate the data of mouse #1 and opened symbols indicate mouse #2 (mean ± SEM). **Figure S3.** HCN1 levels in the EC-rich region of the brains of $X11^{+/+}$/$X11L^{+/+}$ and X11s mutant mice. (***A***) Isolation of the EC-rich region from a horizontal slice (300 μm thick) of murine brain. Brain slices from 13-week-old $X11^{+/+}$/$X11L^{+/+}$, $X11^{+/+}$/$X11L^{-/-}$, $X11^{-/-}$/$X11L^{+/+}$, and $X11^{-/-}$/$X11L^{-/-}$ mice were prepared in ice-cold PBS using a vibratome (VT1200S; Leica) (left panel). The EC-rich region (EC) was separated from each slice as indicated (right panel). (***B, C***) Quantification of HCN1 in the EC-rich region. Horizontal slices were homogenized in eight volumes of radioimmune precipitation assay buffer containing 0.5% (w/v) SDS and a protease inhibitor mixture (5 μg/ml chymostatin, 5 μg/ml leupeptin, and 5 μg/ml pepstatin), subjected to sonication on ice, and centrifuged at 20,000 × g for 10 min at 4°C. (*B*) The resulting supernatants (each containing 10 μg protein) were analyzed by SDS-PAGE on 7.5% (w/v) polyacrylamide gels, followed by immunoblotting with anti-HCN1, anti-X11, anti-X11L, and anti-tubulin antibodies (n = 4). (*C*) The HCN1 level was normalized to the tubulin level to give the relative HCN1/tubulin ratio for each genotype (mean ± SEM, n = 4). **Figure S4.** Altered distribution of the HCN channel in $X11^{-/-}$/$X11L^{-/-}$ mice. (***A***) Low-power images of horizontal brain sections from 13-week-old wild type ($X11^{+/+}$/$X11L^{+/+}$: *upper panels*) and $X11^{-/-}$/$X11L^{-/-}$ (*Lower panels*) mutant mice were immunostained with an anti-HCN1 antibody (n=3). Scale bar, 300 μm. (***B***) Representative high-resolution images of horizontal brain sections from 13-week-old $X11^{+/+}$/$X11L^{+/+}$ (*a, c*) and $X11^{-/-}$/$X11L^{-/-}$ (*b, d*) mice were subjected to immunostaining with an anti-HCN1 antibody (*a, b*) and Nissl stain (*c, d*). (***C***) Quantitative analysis of HCN1 immunoreactivity in the EC of 13-week-old wild type ($X11^{+/+}$/$X11L^{+/+}$) and $X11^{-/-}$/$X11L^{-/-}$ mutant mice. The intensity of the HCN1 immunoreactivity in the areas enclosed by the open boxes in *A* was measured using NIH Image J software. Scale bar, 50 μm. **Figure S5.** Complex formation of HCN1 with APP in N2a cells treated with ZD7288. FLAG-APP and HCN1 were transiently overexpressed in N2a cells (~1 × 10^6) with (+) or without (–) 10 μM ZD7288. To standardize the amount of plasmid transfected into the cells, an empty vector (–) was added to yield 1.2 μg of plasmid in total. The cell lysates were subjected to immunoprecipitation with anti-FLAG M2 antibody. Immunocomplexes were detected by immunoblotting with anti-HCN1 and anti-FLAG antibodies. **Figure S6.** Covariance analysis of various protein levels in the brain of cynomolgus monkeys. (*A–H*) Levels of HCN1, APP, Aβ40, and Aβ42 in the brain (superior temporal gyrus) of 4–37-year-old cynomolgus monkeys were quantified by immunoblotting and sELISA assay. Protein levels were normalized to tubulin levels or to tissue weight to give the relative protein/tubulin ratio for immunoblotting and the relative protein/tissue weight ratio for sELISA. (***A***) Correlation between age and APP level (n = 39, r = 0.8156, ****$p < 0.0001$). (***B***) Correlation between HCN1 and APP levels (n = 39, r = −0.3796, **$p = 0.0086$). (***C, D***) Correlation between HCN1 and Aβ40 levels (n = 39, r = −0.2878, *$p = 0.0421$). An enlarged view of (*C*) in the 0 to 1,000 *f* mol/mg tissue range is shown in (*D*) (***E, F***) Correlation between HCN1 and Aβ42 levels (n = 39, r = −0.2913, *$p = 0.0401$). An enlarged view of (*E*) in the 0 to 400 *f* mol/mg tissue range is shown in (*F*). (***G***) Correlation between APP and Aβ40 (n = 39, r = 0.2993, $p = 0.072$). (***H***) Correlation between APP and Aβ42 levels (n = 39, r = 0.3714, *$p = 0.0236$). Statistical analysis was performed using the two-tailed Pearson's correlation coefficient. **Figure S7.** Specificity of the polyclonal goat anti-HCN1 antibody. (***A***) Competition analysis using glutathione-S-transferase (GST) fused to the 60-amino acid carboxyl terminal region of murine HCN1 (mHCN1 C60). This region of the protein contains the epitope for the goat anti-HCN1 antibody used in this study (sc-19706: Santa Cruz Biotechnology). Brain lysates (10 μg protein) derived from $HCN1^{+/+}$ and $HCN1^{-/-}$ mice and cynomolgus monkeys were subjected to immunoblot analysis. The anti-HCN1 antibody was pre-incubated with 20 μg GST alone or GST-mHCN1 C60 recombinant protein at 4°C for 2 h. The pre-incubated antibody was then reacted with the immunoblots. HCN1 was detected in $HCN1^{+/+}$ mouse and monkey brains when the antibody was pre-incubated with GST alone, but not when the antibody was pre-incubated with GST-mHCN1 C60. (***B***) Titer comparison between anti-HCN1 antibodies. Brain lysates (10 μg protein) were subjected to immunoblot analysis with two commercial anti-HCN1 antibodies (sc-19706, Santa Cruz Biotechnology; and AB5884, Millipore). (***C***) Specificity of goat anti-HCN1 antibody (sc-19706) for immunohistochemical analysis. (***a, b***) Representative images of horizontal brain sections showing the hippocampal formation in 13-week-old $HCN1^{+/+}$ (*a*) and $HCN1^{-/-}$ (*b*) mice stained with goat anti-HCN1 antibody, followed by donkey anti-goat IgG coupled with FITC. (***c, d***) Magnified view of the squares in (***a***) and (***b***). HCN1 signals (green) observed in $HCN1^{+/+}$ mice were absent in $HCN1^{-/-}$ mice. Nuclei counter-stained with DAPI are shown in blue. Scale bars, 300 μm (*a, b*), 50 μm (*c, d*).

Additional file 2: Movie S1. Spontaneous epileptic seizures in $X11^{-/-}$/$X11L^{-/-}$ mice. The electrocorticogram of Supplementary Figure S1 and Movie S3 were simultaneously recorded.

Additional file 3: Movie S2. Spontaneous epileptic seizures in $X11^{-/-}$/$X11L^{-/-}$ mice. The electrocorticogram of Supplementary Figure S1 and Movie S3 were simultaneously recorded.

Additional file 4: Movie S3. Spontaneous epileptic seizures in $X11^{-/-}$/$X11L^{-/-}$ mice. The electrocorticogram of Supplementary Figure S1 and Movie S3 were simultaneously recorded.

Abbreviations

ACSF: Artificial cerebrospinal fluid; AD: Alzheimer's disease; APP: Amyloid precursor protein; Aβ: Amyloid β peptide; DG: Dentate gyrus; EC: Entorhinal cortex; FBS: Fetal bovine serum; HCN channel: Hyperpolarization-activated cyclic nucleotide gated channel; Ih current: Hyperpolarization-activated current; PBS: Phosphate buffered saline; sAPP: Soluble APP; SDS: Sodium dodecyl sulfate; sELISA: Sandwich ELISA; SDS-PAGE: SDS polyacrylamide gel electrophoresis; TBS: Tris buffere saline; X11L: X11-like; X11L2: X11-like2; X11s: X11 proteins.

Competing interests

The authors declare no competing interests.

Authors' contributions

YS, TI, GZ, MO, KI, SK and TS generated the hypotheses for the mouse, monkey and human projects. YS and TS drafted the manuscript. YS, TI, GZ, MO, MN, SK, RS, KI, and TS edited the manuscript and contributed to discussion. YS and NK performed the biochemical and histochemical analyses for the mouse and monkey studies. YS, MN and SM performed biochemical analyses for the human study. TI and KI conducted electrophysiological analyses for the mouse study. YS, GZ, MO and SK performed electroencephalogram recordings. MN and NK provided monkey tissues, and SM provided human tissues. All authors read and approved the final manuscript.

Acknowledgements

This study was supported in part by a Grant-in-Aid for Research Activity Start-up (21890002) and by a Grant-in-Aid for Young Scientists (B) (23790069) from the Japan Society for the Promotion of Science (JSPS) to YS. YS was also supported by the Akiyama Life Science Foundation and the Regional R&D Proposal-Based Program from the Northern Advancement Center for Science & Technology of Hokkaido, Japan. TS was supported in part by Grants-in-aid for Scientific Research (2339001, 2311370, 22659011) from the Ministry of Education, Culture, Sports, Science and Technology (MEXT) of Japan, and by a grant from the Ministry of Health, Labor and Welfare (MHLW) of Japan.

Author details

[1]Laboratory of Neuroscience, Graduate School of Pharmaceutical Sciences, Hokkaido University, Kita12-Nishi6, Kita-ku, Sapporo 060-0812, Japan. [2]Laboratory of Neurobiophysics, Graduate School of Medicine, Dentistry and Pharmaceutical Sciences, Okayama University, Okayama 700-8530, Japan. [3]Department of Psychiatry, The First Affiliated Hospital of China Medical University, Shenyang 110001, China. [4]Division of Neuroscience, Graduate School of Medicine, Mie University, Tsu 514-8507, Japan. [5]Molecular Neuroscience Research Center, Shiga University of Medical Science, Otsu 520-2192, Japan. [6]Laboratory of Disease Control, Tsukuba Primate Research Center, National Institute of Biomedical Innovation, Tsukuba 305-0843, Japan. [7]Department of Neuropathology, Tokyo Metropolitan Institute of Gerontology, Itabashi-ku, Tokyo 173-0015, Japan. [8]Brain Bank for Aging Research, Tokyo Metropolitan Institute of Gerontology, Itabashi-ku, Tokyo 173-0015, Japan. [9]Departments of Neuropsychiatry, Graduate School of Medicine, Hirosaki University, Hirosaki 036-8562, Japan. [10]Division of Cerebral Structure, National Institute for Physiological Sciences, Okazaki 444-8585, Japan. [11]Department of Information Physiology, National Institute for Physiological Sciences, Okazaki 444-8787, Japan.

Received: 12 April 2012 Accepted: 27 September 2012
Published: 3 October 2012

References

1. Selkoe DJ: **Alzheimer's disease is a synaptic failure.** *Science* 2002, **298**:789–791.
2. Hauser WA, Morris ML, Heston LL, Anderson VE: **Seizures and myoclonus in patients with Alzheimer's disease.** *Neurology* 1986, **36**:1226–1230.
3. Hesdorffer DC, Hauser WA, Annegers JF, Kokmen E, Rocca WA: **Dementia and adult-onset unprovoked seizures.** *Neurology* 1996, **46**:727–730.
4. Mendez M, Lim G: **Seizures in elderly patients with dementia: epidemiology and management.** *Drugs Aging* 2003, **20**:791–803.
5. Amatniek JC, Hauser WA, DelCastillo Castaneda C, Jacobs DM, *et al*: **Incidence and predictors of seizures in patients with Alzheimer's disease.** *Epilepsia* 2006, **47**:867–872.
6. Lozsadi DA, Larner AJ: **Prevalence and causes of seizures at the time of diagnosis of probable Alzheimer's disease.** *Dement Geriatr Cogn Disord* 2006, **22**:121–124.
7. Marcon G, Giaccone G, Cupidi C, Balestrieri M, Beltrami CA, *et al*: **Neuropathological and clinical phenotype of an Italian Alzheimer family with M239V mutation of presenilin 2 gene.** *J Neuropathol Exp Neurol* 2004, **63**:199–209.
8. Kamenetz F, Tomita T, Hsieh H, Seabrook G, Borchelt D, *et al*: **APP processing and synaptic function.** *Neuron* 2003, **37**:925–937.
9. Cirrito JR, Yamada KA, Finn MB, Sloviter RS, Bales KR, *et al*: **Synaptic activity regulates interstitial fluid amyloid-beta levels *in vivo*.** *Neuron* 2005, **48**:913–922.
10. Cirrito JR, Kang JE, Lee J, Stewart FR, Verges DK, *et al*: **Endocytosis is required for synaptic activity-dependent release of amyloid-beta *in vivo*.** *Neuron* 2008, **58**:42–51.
11. Postea O, Biel M: **Exploring HCN channels as novel drug targets.** *Nat Rev Drug Discov* 2011, **10**:903–914.
12. Noam Y, Bernald C, Baram TZ: **Towards an integrated view of HCN channel role in epilepsy.** *Curr Opin Neurobiol* 2011, **21**:873–879.
13. Kimura K, Kitano J, Nakajima Y, Nakanishi S: **Hyperpolarization-activated cyclic nucleotide-gated HCN2 cation channel forms a protein assembly with multiple neuronal scaffold proteins in distinct modes of protein-protein interaction.** *Genes Cells* 2004, **9**:631–640.
14. Suzuki T, Nakaya T: **Regulation of amyloid β-protein precursor by phosphorylation and protein interaction.** *J Biol Chem* 2008, **283**:29633–29637.
15. Borg JP, Yang Y, De Taddeo Borg M, Margolis B, Turner RS: **The X11alpha protein slows cellular amyloid precursor protein processing and reduces Abeta40 and Abeta42 secretion.** *J Biol Chem* 1998, **273**:14761–14766.
16. Tomita S, Ozaki T, Taru H, Oguchi S, Takeda S, *et al*: **Interaction of a neuron-specific protein containing PDZ domains with Alzheimer's amyloid precursor protein.** *J Biol Chem* 1999, **274**:2243–2254.
17. Lee JH, Lau KF, Perkinton MS, Standen CL, Shemilt SJ, *et al*: **The Neuronal Adaptor Protein X11α Reduces Aβ Levels in the Brains of Alzheimer's APPswe Tg2576 Transgenic Mice.** *J Biol Chem* 2003, **278**:47025–47029.
18. Lee JH, Lau KF, Perkinton MS, Standen CL, Rogelj B, *et al*: **The neuronal adaptor protein X11beta reduces amyloid beta-protein levels and amyloid plaque formation in the brains of transgenic mice.** *J Biol Chem* 2004, **279**:49099–49104.
19. Mitchell JC, Ariff BB, Yates DM, Lau KF, Perkinton MS, *et al*: **X11beta rescues memory and long-term potentiation deficits in Alzheimer's disease APPswe Tg2576 mice.** *Hum Mol Genet* 2009, **18**:4492–4500.
20. Sano Y, Syuzo-Takabatake A, Nakaya T, Saito Y, Tomita S, *et al*: **Enhanced amyloidogenic metabolism of the amyloid beta-protein precursor in the X11L-deficient mouse brain.** *J Biol Chem* 2006, **281**:37853–37860.
21. Saito Y, Sano Y, Vassar R, Gandy S, Nakaya T, *et al*: **X11 proteins regulate the translocation of amyloid beta-protein precursor (APP) into detergent-resistant membrane and suppress the amyloidogenic cleavage of APP by beta-site-cleaving enzyme in brain.** *J Biol Chem* 2008, **283**:35763–35771.
22. Kondo M, Shiono M, Itoh G, Takei N, Matsushima T, *et al*: **Increased amyloidogenic processing of transgenic human APP in X11-like deficient mouse brain.** *Mol Neurodegener* 2010, **5**:35.
23. Morimoto K, Fahnestock M, Racine RJ: **Kindling and status epilepticus models of epilepsy: rewiring the brain.** *Prog Neurobiol* 2004, **73**:1–60.
24. van Strien NM, Cappaert NL, Witter MP: **The anatomy of memory: an interactive overview of the parahippocampal-hippocampal network.** *Nat Rev Neurosci* 2009, **10**:272–282.
25. Notomi T, Shigemoto R: **Immunohistochemical localization of Ih channel subunits, HCN1-4, in the rat brain.** *J Comp Neurol* 2004, **471**:241–276.
26. Ludwig A, Budde T, Stieber J, Moosmang S, Wahl C, *et al*: **Absence epilepsy and sinus dysrhythmia in mice lacking the pacemaker channel HCN2.** *EMBO J* 2003, **22**:216–224.
27. Huang Z, Walker MC, Shah MM: **Loss of dendritic HCN1 subunits enhances cortical excitability and epileptogenesis.** *J Neurosci* 2009, **29**:10979–10988.